Dispersion of gyrotactic micro-organisms in pipe flows

Weiquan Jiang[1] **and Guoqian Chen**[1,†]

[1]Laboratory of Systems Ecology and Sustainability Science, College of Engineering, Peking University, Beijing 100871, PR China

The transport of motile micro-organisms exhibits rich and complex phenomena, of significance to various biological and environmental applications. For dilute suspensions of gyrotactic algae dispersing in vertical pipe flows, previous studies obtained only approximate values for the overall drift and dispersivity in the longitudinal direction, using two-step averaging methods with the Pedley–Kessler (PK) model and the generalized Taylor dispersion (GTD) model. These two-step methods impose restrictive assumptions: both the swimming Péclet number and the variation of shear rates relative to swimming must be sufficiently small. Thus, it is difficult to analyse the gyrotactic dispersion process in the 'breakdown' parameter region. Following a recent study of Jiang & Chen (*J. Fluid Mech.*, vol. 877, 2019, pp. 1–34), this paper applies the integrated and precise one-step GTD method to study the overall dispersion process and performs a quantitative test for the applicability of two-step methods. An appropriate function basis for series expansions in the GTD method is proposed to deal with reflective boundary conditions imposed at the tube wall. Detailed results for *Chlamydomonas nivalis* are presented to illustrate the influence of the gyrotactic focusing on the overall dispersion process, for both downwelling and upwelling flows. The overall drift above the mean flow increases monotonically with the flow rate. However, the overall dispersivity will first decrease, then increase, and finally saturate as the flow rate increases, due to a combined effect of gyrotaxis, swimming and convection. Shear alignments of prolate cells will weaken the focusing, and thus reduce the drift and enhance the dispersivity. The predictions by two-step methods with the PK and GTD models are found to be successful inside their required parameter region. Within the 'breakdown' region, the two-step GTD method still gives reasonable results for the local distribution and the drift, but fails in the predictions of dispersivity.

Key words: micro-organism dynamics, swimming/flying, mixing and dispersion

1. Introduction

The transport of micro-organisms is a crucial issue for a wide range of biological and environmental applications, such as algae cultivation (Posten 2009; Liao *et al.*

† Email address for correspondence: gqchen@pku.edu.cn

2014; Acién *et al.* 2017), biofuels (Chisti 2007; Mata, Martins & Caetano 2010; Stephenson *et al.* 2010), bio-remediation (Muñoz & Guieysse 2006; Suresh Kumar *et al.* 2015) and wetlands (Zeng & Pedley 2018; Zeng *et al.* 2019; Yang *et al.* 2020). Suspensions of motile micro-organisms exhibit much richer and more complex phenomena than those of passive particles (Saintillan 2018), including collective behaviour (Pedley & Kessler 1992; Ishikawa & Pedley 2007, 2008; Pedley 2010*a*; Marchetti *et al.* 2013), upstream swimming (Hill *et al.* 2007; Rusconi & Stocker 2015; Mathijssen *et al.* 2016) and wall accumulation (Rothschild 1963; Berke *et al.* 2008; Elgeti & Gompper 2013).

Besides the self-propulsion effect, taxes of micro-organisms, such as gravitaxis (in response to gravity), chemotaxis (chemical gradients) and phototaxis (light) (Pedley & Kessler 1992; Bees & Croze 2014; Goldstein 2015), also play a significant role in transport processes. In shear flows, the phenomenon induced by gyrotaxis is of considerable interest, which is a combined effect of the gravitational torque (by gravitaxis (Fenchel & Finlay 1984, 1986)) and the viscous torque (by shear (Jeffery 1922)). The imposed flow induces a gyrotactic bias for micro-organisms, e.g. bottom-heavy algae like *Chlamydomonas nivalis* and *Dunaliella*. One of the most well-known phenomena is the gyrotactic focusing of algae in vertical pipe flows (Kessler 1984, 1985, 1986). Cells accumulate at the centre of the tube in a downwelling flow and migrate to the walls in an upwelling flow (Pedley & Kessler 1992). This self-focus phenomenon can also be induced by phototaxis in a horizontal pipe flow (Garcia, Rafaï & Peyla 2013; Martin *et al.* 2016), called photofocusing. The gyrotactic nature can lead to instability in bioconvection (Childress, Levandowsky & Spiegel 1975; Pedley, Hill & Kessler 1988; Pedley 2010*b*; Hwang & Pedley 2014*a*). In coastal ocean, gyrotaxis plays the fundamental role in the formation of thin layers of phytoplankton, called gyrotactic trapping (Durham, Kessler & Stocker 2009; Durham & Stocker 2012; Ishikawa 2012; Cencini *et al.* 2019).

Dispersion of gyrotactic micro-organisms in confined flows has also been intensively investigated. The pioneering work by Bees & Croze (2010) has extended the classic Taylor–Aris dispersion theory (Taylor 1953, 1954; Aris 1956) of passive particles in pipe flows to the case of gyrotactic particles. The convection–diffusion equation for a passive solute is replaced by a new and effective one for active particles, originally proposed by Pedley & Kessler (1990). This new continuum model, referred to as the Pedley–Kessler (PK) model, is a simplification of the Smoluchowski equation (Doi & Edwards 1988), i.e. the transport equation in the six-dimensional position–orientation space (Hwang & Pedley 2014*a*). The effective drift and dispersivity tensor for the convection–diffusion equation in the position space is approximated by a Fokker–Planck (FP) equation (Risken 1996) for the swimming direction of active particles in the orientation space (Pedley & Kessler 1992). Based on the PK model (also called the FP model), Bees & Croze (2010) analytically derived the overall drift and effective dispersivity for macrotransport in the longitudinal direction of a pipe flow and found significant differences from the passive case due to the focusing.

Apart from the PK model, the generalized Taylor dispersion (GTD) theory (Brenner 1982; Frankel & Brenner 1989) has also been applied to study the macrotransport of gyrotactic micro-organisms in confined flows. Taking the orientation as the local space, with the position as the global space, the fundamental work by Hill & Bees (2002) extended the GTD of passive Brownian particles in unbounded homogeneous shear flow (Frankel & Brenner 1991, 1993) to the case of gyrotactic spherical cells. Performing the mean operation on the local orientation space, the effective drift and dispersivity tensor for the convection–diffusion equation in the position space

were calculated and extended to the case of ellipsoidal cells by Manela & Frankel (2003). Bearon, Hazel & Thorn (2011) made a key attempt to widen the range of applications of the GTD model to flows with variable shear rates. Instead of using the PK model in Bees & Croze (2010), the effective dispersivity tensor at each position is approximated by the GTD model with the case of an imaginary unbounded homogeneous shear flow with the same shear as the local one. Next, using this new effective convection–diffusion equation in the position space as the first step, Bearon, Bees & Croze (2012) performed a second mean operation on the confined section using the classic Taylor–Aris dispersion theory (Taylor 1953; Aris 1956; Bees & Croze 2010) and obtained the overall drift and dispersivity in the longitudinal direction. For dilute suspensions in vertical downwelling pipe flow, they found more reasonable dispersion results, compared with those of Bees & Croze (2010) using the PK model. Later, Croze *et al.* (2013) extended both the PK and GTD models to the dispersion of algae in laminar and turbulent channel flows, and compared the theoretical predictions with numerical simulations by the random walk method. Recently, an experimental test for these models was taken by Croze, Bearon & Bees (2017). When the shear rate is large, both the numerical and experimental results found good agreements with the GTD model but poor agreements with the PK model.

However, both the PK and GTD models for the convection–diffusion equation have made restrictive assumptions and thus their applications are limited (Bearon *et al.* 2011). Note that, although in the second step, the overall drift and dispersivity for the macrotransport in the longitudinal direction of the confined flow can be analytically derived by the classic Taylor–Aris dispersion theory (Bees & Croze 2010) based on the effective convection–diffusion equation, the effective equation itself obtained in the first step is only a simplified approximation of the complete transport equation of the phase space (position–orientation) into the lower-dimensional position space. It requires that the swimming Péclet number $Pe_s \ll 1$. Namely, the time scale that the swimmer takes to rotate in the orientation space is much less than the time it takes to swim across the tube (Bearon *et al.* 2011; Jiang & Chen 2019*a*), and thus the boundary effect can also be neglected. Additionally, the PK model neglects the local spatial distribution by the cell locomotion in a shear flow, which is valid only for weak shear (Croze *et al.* 2017). Although the GTD model incorporates the local shear as unbounded homogeneous shear, the relative variation of the shear rates must also be small enough to be neglected. In fact, discrepancies in the local distribution, overall drift and overall dispersivity between the predictions by the two models and numerical simulations (Bearon *et al.* 2011; Croze *et al.* 2013) have been demonstrated outside the required parameter region.

To analytically derive the overall drift and dispersivity, recently, a more integrated one-step approach has been devised in place of the above two-step methods (Jiang & Chen 2019*a*). Unlike the two-step GTD method, this one-step method sets both the orientation space and confined section of the position space together as the local space, and thus the longitudinal coordinate as a one-dimensional global space. Fully utilizing the GTD theory, the mean operation on the local space is performed only once, then the overall dispersion coefficients can be obtained, without introducing the effective convection–diffusion equation in the position space as an approximation in the two-step methods with the PK or GTD models. Therefore, the one-step method can be analytically accurate and strongly adaptable for applications. Jiang & Chen (2019*a*) gave elementary examples of dilute suspensions of active particles dispersing in channel flows. The case of gyrotactic micro-organisms has not yet been investigated.

In this work we apply the one-step method to study the dispersion of dilute suspensions of gyrotactic micro-organisms in vertical pipe flows, and illustrate the influence of the gyrotactic focusing on the dispersion process. It is of considerable interest to perform a quantitative test for the applicability of the two-step methods with the GTD and PK models. For the transport problem formulated in §2, the one-step GTD method is applied in §3. The key is to solve the local transport equation equipped with reflective boundary conditions that are an idealization assuming elastic collisions between particles and solid boundaries (Bearon *et al.* 2011; Volpe, Gigan & Volpe 2014; Jakuszeit, Croze & Bell 2019). In the paper by Jiang & Chen (2019*a*), the reflection principle in the random walk theory is used to obtain the local distribution with the Galerkin method, by reflecting the channel flow field. However, for the pipe flow, it is not applicable because the geometric shape of the cross-section is a circle. To overcome this, we propose new reflection basis functions on the local space for the series expansion. In §4, the overall dispersion of the classic case for the gyrotactic focusing is illustrated, for both downwelling and upwelling flows.

2. Formulation of transport problem

2.1. *Governing equations*

Consider the probability density function (p.d.f.) P of motile micro-organisms in the position–orientation space $(\boldsymbol{R}^*, \boldsymbol{p})$, where $\boldsymbol{R}^*$ is the position vector and $\boldsymbol{p}$ is the orientation vector. The conservation equation for P can be given by the Smoluchowski equation (Doi & Edwards 1988) as

$$\frac{\partial P}{\partial t^*} + \boldsymbol{\nabla}_R^* \cdot \boldsymbol{J}_R^* + \boldsymbol{\nabla}_p \cdot \boldsymbol{j}_p^* = 0, \tag{2.1}$$

where $\boldsymbol{\nabla}_R^*$ denotes the gradient operator in the position space, $\boldsymbol{\nabla}_p$ is that in the swimming orientation space, t^* is time,

$$\boldsymbol{J}_R^* = [\boldsymbol{U}^*(\boldsymbol{R}^*) + V_s^* \boldsymbol{p}]P - D_t^* \boldsymbol{\nabla}_R^* P \tag{2.2}$$

is the position-space flux and

$$\boldsymbol{j}_p^* = \dot{\boldsymbol{p}}^* P - D_r^* \boldsymbol{\nabla}_p P \tag{2.3}$$

is the orientation-space flux density, with $\boldsymbol{U}^*$ the velocity of the external flow, V_s^* the mean swimming speed of the particles, D_t^* the translational diffusivity and D_r^* the rotational diffusivity. The rate of change of swimming direction is

$$\dot{\boldsymbol{p}}^* = \boldsymbol{\Omega}_a^* \times \boldsymbol{p}, \tag{2.4}$$

where a dot above a variable denotes the time derivative and $\boldsymbol{\Omega}_a^*$ is the total angular velocity of the particle. For gyrotactic micro-organisms (Jeffery 1922; Leal & Hinch 1972; Pedley & Kessler 1992)

$$\boldsymbol{\Omega}_a^* = \frac{1}{2B^*} \boldsymbol{p} \times \boldsymbol{k} + \frac{1}{2}\boldsymbol{\omega}^* + \alpha_0[\boldsymbol{p} \times (\boldsymbol{E}^* \cdot \boldsymbol{p})], \tag{2.5}$$

where B^* is the gyrotactic time scale, $\boldsymbol{k}$ is the unit vector pointing vertically upwards,

$$\boldsymbol{\omega}^* = \boldsymbol{\nabla}_R^* \times \boldsymbol{U}^* \tag{2.6}$$

is the ambient vorticity,

$$\boldsymbol{E}^* = \tfrac{1}{2}[\boldsymbol{\nabla}_R^* \boldsymbol{U}^* + (\boldsymbol{\nabla}_R^* \boldsymbol{U}^*)^{\mathrm{T}}] \tag{2.7}$$

is the rate-of-strain tensor and α_0 is the shape factor of the particle, with $\alpha_0 = 0$ for a sphere and $\alpha_0 = 1$ for an infinitely thin rod-like particle.
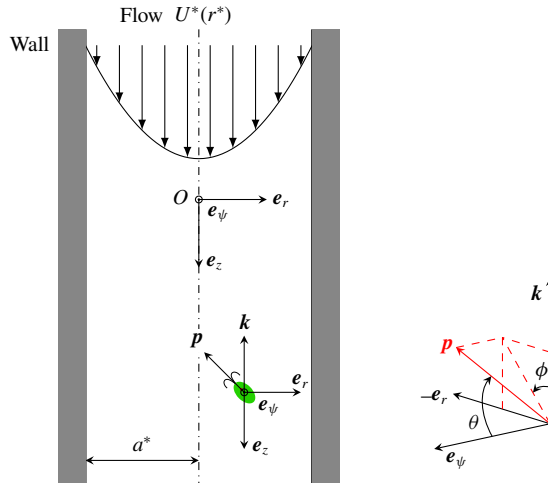
FIGURE 1. Sketch of a gyrotactic micro-organism swimming in a vertical downwelling pipe flow. Here p is the swimming direction with polar angle θ and azimuthal angle ϕ.

2.2. Dimensionless formulation

For a dilute suspension of gyrotactic micro-organisms in a vertical pipe flow with radius a^*, as shown in figure 1, we employ cylindrical coordinates (r^*, ψ, z^*) in the position space with unit vectors e_r, e_ψ and e_z, so that

$$U^* = U^*(r^*)e_z, \tag{2.8}$$

where U^* is the flow speed.

In the orientation space, we employ spherical coordinates (ρ, θ, ϕ) with unit vectors e_ρ, e_θ and e_ϕ. Here θ is the polar angle between p and e_ψ, and ϕ is the azimuthal angle between $-e_z$ and the projection of p onto the z–r plane. Then the swimming direction is

$$p = e_\rho = p_r(\theta, \phi)e_r + p_\psi(\theta, \phi)e_\psi + p_z(\theta, \phi)e_z, \tag{2.9}$$

where

$$p_r = -\sin\theta\sin\phi, \quad p_\psi = \cos\theta, \quad p_z = -\sin\theta\cos\phi. \tag{2.10a-c}$$

Dimensionless variables and parameters are introduced:

$$\left.\begin{array}{c} t = t^* D_r^*, \quad r = \dfrac{r^*}{a^*}, \quad z = \dfrac{z^*}{a^*} - Pe_f t, \quad U = \dfrac{U^*}{U_m^*} - 1, \\[2mm] Pe_s = \dfrac{V_s^*}{D_r^* a^*}, \quad Pe_f = \dfrac{U_m^*}{D_r^* a^*}, \quad D_t = \dfrac{D_t^*}{D_r^* a^{*2}}, \quad \lambda = \dfrac{1}{2B^* D_r^*}. \end{array}\right\} \tag{2.11}$$

The frame of reference is transformed to that moving with the mean flow U_m^*,

$$U_m^* \triangleq \frac{1}{a^{*2}} \int_0^{a^*} 2r^* U^*(r^*)\, dr^*, \tag{2.12}$$

and thus U is the flow deviation from the mean. In the above, Pe_s is the swimming Péclet number for the rotational diffusion, Pe_f is the flow Péclet number, D_t is the ratio of the translational diffusivity to the rotational diffusivity, and λ is the bias parameter.

In the current coordinate system, the conservation equation (2.1) becomes

$$\frac{\partial P}{\partial t} + \nabla_R \cdot [(Pe_f U e_z + Pe_s p)P - D_t \nabla_R P] + \nabla_p \cdot (\dot{p}_r P - \nabla_p P) = 0, \quad (2.13)$$

where $\nabla_R = e_r(\partial/\partial r) + e_\psi(1/r)(\partial/\partial\psi) + e_z(\partial/\partial z)$, $\nabla_p = e_\theta(\partial/\partial\theta) + e_\phi(1/\sin\theta)(\partial/\partial\phi)$, and the relative rate of change of swimming direction

$$\dot{p}_r = \dot{p} - \dot{p}_c, \quad (2.14)$$

with the Coriolis effect $\dot{p}_c = \dot{\psi} e_z \times p$ and $\dot{\psi} = (Pe_s p_\psi/r)$. Let

$$\dot{p}_r = \dot{\theta}\, e_\theta + \dot{\phi}\sin\theta\, e_\phi, \quad (2.15)$$

then

$$\dot{\theta} = \lambda\cos\phi\cos\theta + \frac{\alpha_0 Pe_f}{4}\frac{\partial U}{\partial r}\sin 2\theta\sin 2\phi - \frac{Pe_s}{r}\cos\theta\sin\phi, \quad (2.16)$$

$$\dot{\phi} = -\lambda\frac{\sin\phi}{\sin\theta} - \frac{Pe_f}{2}\frac{\partial U}{\partial r}(1 - \alpha_0\cos 2\phi) - \frac{Pe_s}{r}\cos\theta\cot\theta\cos\phi. \quad (2.17)$$

Note that when $\lambda = 0$ (without the gyrotactic bias), $\dot{\theta}$ and $\dot{\phi}$ correspond to the results of Zöttl & Stark (2013).

It is assumed that collisions between particles and solid boundaries are perfectly elastic (Bearon *et al.* 2011; Ezhilan, Pahlavan & Saintillan 2012; Volpe *et al.* 2014; Jakuszeit *et al.* 2019). Thus, reflective boundary conditions at pipe walls are imposed as

$$P(1, \psi, z, \theta, \phi, t) = P(1, \psi, z, \theta, -\phi, t), \quad (2.18)$$

$$\frac{\partial P}{\partial r}(1, \psi, z, \theta, \phi, t) = -\frac{\partial P}{\partial r}(1, \psi, z, \theta, -\phi, t), \quad (2.19)$$

ensuring zero total wall-normal probability flux through the walls,

$$0 = \int_0^\pi \sin\theta\, \mathrm{d}\theta \int_0^{2\pi} \mathrm{d}\phi\, (e_r \cdot J_R)$$
$$= \int_0^\pi \sin\theta\, \mathrm{d}\theta \int_{-\pi}^\pi \mathrm{d}\phi \left(-Pe_s\sin\theta\sin\phi\, P - D_t\frac{\partial P}{\partial r}\right). \quad (2.20)$$

Note that previous studies (Bearon *et al.* 2011; Ezhilan & Saintillan 2015; Jiang & Chen 2019*a*) only considered (2.18), with the swimming flux balanced by reflections. In fact, the transitional diffusive flux is also balanced and thus satisfies (2.19).

At the cylindrical coordinate origin ($r = 0$), a finite probability condition is stated as

$$P|_{r=0} \neq \infty. \quad (2.21)$$

Periodic boundary conditions for ψ are

$$\left.\begin{array}{c} P|_{\psi=0} = P|_{\psi=2\pi}, \\ \left.\dfrac{\partial P}{\partial \psi}\right|_{\psi=0} = \left.\dfrac{\partial P}{\partial \psi}\right|_{\psi=2\pi}. \end{array}\right\} \tag{2.22}$$

In the orientation dimension, a finite probability condition for θ reads as

$$P|_{\theta=\pi/2} \neq \infty, \quad P|_{\theta=-\pi/2} \neq \infty, \tag{2.23a,b}$$

and periodic boundary conditions for ϕ are

$$\left.\begin{array}{c} P|_{\phi=\pi} = P|_{\phi=-\pi}, \\ \left.\dfrac{\partial P}{\partial \phi}\right|_{\phi=\pi} = \left.\dfrac{\partial P}{\partial \phi}\right|_{\phi=-\pi}. \end{array}\right\} \tag{2.24}$$

An initial probability distribution $P^{(0)}$ is prescribed

$$P|_{t=0} = P^{(0)}(r, \psi, z, \theta, \phi). \tag{2.25}$$

3. Solutions for generalized Taylor dispersion model

3.1. *Local and global spaces*

For pipe flows, the longitudinal scale is much larger than the transverse scale (Wu & Chen 2014). The overall dispersion in the longitudinal direction is of interest. To obtain the overall drift and dispersivity, one can apply the GTD theory (Brenner 1982; Frankel & Brenner 1989).

Following Jiang & Chen (2019*a*), the one-step GTD method is employed: the unbounded longitudinal coordinate z is chosen as the global space variable $\boldsymbol{Q} = (z)$, while the local space $\boldsymbol{q} = (r, \psi, \theta, \phi)$. The transport equation (2.13) is recast as

$$\frac{\partial P}{\partial t} + [Pe_f U(r) - Pe_s \sin\theta \cos\phi] \frac{\partial P}{\partial z} - D_t \frac{\partial^2 P}{\partial z^2} + \mathcal{L}P = 0, \tag{3.1}$$

where $\mathcal{L}$ is an operator defined in the local space $\boldsymbol{q}$, and explicitly

$$\mathcal{L}P \triangleq -\frac{Pe_s \sin\theta \sin\phi}{r} \frac{\partial(rP)}{\partial r} + \frac{Pe_s \cos\theta}{r} \frac{\partial P}{\partial \psi} - D_t \left[\frac{1}{r} \frac{\partial}{\partial r} \left(r \frac{\partial P}{\partial r} \right) + \frac{1}{r^2} \frac{\partial^2 P}{\partial \psi^2} \right]$$
$$+ \frac{1}{\sin\theta} \frac{\partial(\dot\theta \sin\theta\, P)}{\partial \theta} + \frac{\partial(\dot\phi P)}{\partial \phi} - \frac{1}{\sin\theta} \frac{\partial}{\partial \theta} \left(\sin\theta \frac{\partial P}{\partial \theta} \right) - \frac{1}{\sin^2\theta} \frac{\partial^2 P}{\partial \phi^2}. \tag{3.2}$$

We use angle brackets to denote the integration over the local space (a cross-section in the phase space), e.g.

$$\langle P \rangle \triangleq \int_0^1 r\, \mathrm{d}r \int_0^{2\pi} \mathrm{d}\psi \int_0^\pi \sin\theta\, \mathrm{d}\theta \int_0^{2\pi} \mathrm{d}\phi\, P(r, \psi, z, \theta, \phi, t) \tag{3.3}$$

represents the cross-sectional mean concentration of micro-organisms in the longitudinal direction.

3.2. *Long-time asymptotic distribution in local space*

First, we consider the long-time asymptotic state of the zeroth-order longitudinal moment of P,

$$P_0^\infty(r, \psi, \theta, \phi) \triangleq \lim_{t \to \infty} \left(\int_{-\infty}^{+\infty} P(r, \psi, z, \theta, \phi, t) \, dz \right), \tag{3.4}$$

i.e. a steady local distribution in the local space. According to the GTD theory (Brenner 1982; Frankel & Brenner 1989), P_0^∞ satisfies

$$\mathcal{L}P_0^\infty = 0. \tag{3.5}$$

The form of the boundary conditions for P_0^∞ is the same as those for P, i.e. (2.18)–(2.24). Note that the above boundary value problem (BVP) for P_0^∞ is independent of ψ.

One can solve for P_0^∞ by the Galerkin method (Doi & Edwards 1978; Hill & Bees 2002; Manela & Frankel 2003), expanding in cylindrical and spherical harmonics. To perform the series expansion, first, we seek the basis functions satisfying the reflective boundary conditions.

3.2.1. *Reflection basis functions*

One can use the eigenfunctions of the Laplace operator,

$$\Delta_q = \frac{1}{r} \frac{\partial}{\partial r} \left(r \frac{\partial}{\partial r} \right) + \frac{1}{\sin \theta} \frac{\partial}{\partial \theta} \left(\sin \theta \frac{\partial}{\partial \theta} \right) + \frac{1}{\sin^2 \theta} \frac{\partial^2}{\partial \phi^2}, \tag{3.6}$$

on the local space to find the required basis functions. The inner product for given functions f and g is

$$\langle f, g \rangle \triangleq \int_0^1 r \, dr \int_0^\pi \sin \theta \, d\theta \int_0^{2\pi} d\phi \, f(r, \theta, \phi) g(r, \theta, \phi). \tag{3.7}$$

Note that Δ_q is self-adjoint with the reflective, finite and periodic boundary conditions (2.18)–(2.24). One needs to check the radial term. Integration by parts gives

$$\int_0^1 r \, dr \int_0^\pi \sin \theta \, d\theta \int_0^{2\pi} d\phi \, g \frac{1}{r} \frac{\partial}{\partial r} \left(r \frac{\partial f}{\partial r} \right)$$

$$= \int_0^\pi \sin \theta \, d\theta \int_0^{2\pi} d\phi \left(g r \frac{\partial f}{\partial r} - r f \frac{\partial g}{\partial r} \right) \bigg|_{r=0}^{r=1}$$

$$+ \int_0^1 r \, dr \int_0^\pi \sin \theta \, d\theta \int_0^{2\pi} d\phi \, f \frac{1}{r} \frac{\partial}{\partial r} \left(r \frac{\partial g}{\partial r} \right).$$

The reflection conditions (2.18) and (2.19) ensure that all the boundary terms are equal to zero. Namely,

$$\int_0^\pi \sin \theta \, d\theta \int_0^{2\pi} d\phi \left(r g \frac{\partial f}{\partial r} \right) \bigg|_{r=1} = \int_0^\pi \sin \theta \, d\theta \int_0^{2\pi} d\phi \left(r f \frac{\partial g}{\partial r} \right) \bigg|_{r=1} = 0 \tag{3.8}$$

because both $(\partial f / \partial r(1, \theta, \phi))$ and $(\partial g / \partial r(1, \theta, \phi))$ are odd functions with respect to ϕ.

To construct the eigenfunctions for Δ_q, one can use the spherical harmonics,

$$R^{\mathrm{c}}(r)\sqrt{\frac{2l+1}{4\pi}}\mathrm{P}_l(\cos\theta), \tag{3.9}$$

$$R^{\mathrm{c}}(r)\sqrt{2}\sqrt{\frac{2l+1}{4\pi}\frac{(l-m)!}{(l+m)!}}\cos(m\phi)\mathrm{P}_l^m(\cos\theta), \quad m=1,2,\ldots,l, \tag{3.10}$$

$$R^{\mathrm{s}}(r)\sqrt{2}\sqrt{\frac{2l+1}{4\pi}\frac{(l-m)!}{(l+m)!}}\sin(m\phi)\mathrm{P}_l^m(\cos\theta), \quad m=1,2,\ldots,l, \tag{3.11}$$

where $l=0,1,2,\ldots$, P_l are the Legendre polynomials and P_l^m are the associated Legendre polynomials (Olver *et al.* 2010),

$$\mathrm{P}_l^m(x)=(-1)^m(1-x^2)^{m/2}\frac{\mathrm{d}^m}{\mathrm{d}x^m}\mathrm{P}_l(x), \tag{3.12}$$

with the Condon–Shortley phase $(-1)^m$.

The undetermined functions $R^{\mathrm{c}}(r)$ and $R^{\mathrm{s}}(r)$ satisfy

$$\frac{1}{r}\frac{\partial}{\partial r}\left(r\frac{\partial R(r)}{\partial r}\right)-l(l+1)R(r)=\chi R(r), \tag{3.13}$$

where χ is the eigenvalue for Δ_q. For $R^{\mathrm{c}}(r)$, the reflection conditions (2.18) and (2.19) require

$$\cos(m\phi)R^{\mathrm{c}}(1)=\cos(-m\phi)R^{\mathrm{c}}(1), \quad \forall\ \phi\in[0,2\pi], \tag{3.14}$$

$$\cos(m\phi)\frac{\partial R^{\mathrm{c}}(1)}{\partial r}=-\cos(-m\phi)\frac{\partial R^{\mathrm{c}}(1)}{\partial r}, \quad \forall\ \phi\in[0,2\pi], \tag{3.15}$$

namely,

$$\frac{\partial R^{\mathrm{c}}(1)}{\partial r}=0. \tag{3.16}$$

Therefore, the solution for $R^{\mathrm{c}}(r)$ is

$$R_n^{\mathrm{c}}(r)=\sqrt{2}\frac{\mathrm{J}_0(\sqrt{-\beta_n}r)}{\mathrm{J}_0(\sqrt{-\beta_n})}, \quad n=0,1,2,\ldots, \tag{3.17}$$

where J_0 is the Bessel function of the first kind and β_n is the nth non-negative zero of

$$\frac{\mathrm{dJ}_0}{\mathrm{d}r}(\sqrt{-\beta_n})=\mathrm{J}_1(\sqrt{-\beta_n})=0, \quad n=0,1,2,\ldots. \tag{3.18}$$

Notice that $\beta_0=0$ and $R_0^{\mathrm{c}}(r)=\sqrt{2}$. The corresponding eigenvalue is

$$\chi_{nl}^{\mathrm{c}}=-l(l+1)-\beta_n^2, \quad n=0,1,2,\ldots. \tag{3.19}$$

Similarly, for $R^{\mathrm{s}}(r)$, the reflection conditions (2.18) and (2.19) require

$$\sin(m\phi)R^{\mathrm{s}}(1)=\sin(-m\phi)R^{\mathrm{s}}(1), \quad \forall\ \phi\in[0,2\pi], \tag{3.20}$$

$$\sin(m\phi)\frac{\partial R^{\mathrm{s}}(1)}{\partial r} = -\sin(-m\phi)\frac{\partial R^{\mathrm{s}}(1)}{\partial r}, \quad \forall\ \phi \in [0, 2\pi], \tag{3.21}$$

namely,

$$R^{\mathrm{s}}(1) = 0. \tag{3.22}$$

Therefore, the solution for $R^{\mathrm{s}}(r)$ is

$$R^{\mathrm{s}}(r) = \sqrt{2}\,\frac{\mathrm{J}_0(\sqrt{-\gamma_n}r)}{\mathrm{J}_1(\sqrt{-\gamma_n})}, \quad n = 1, 2, \ldots, \tag{3.23}$$

where γ_n is the nth zero of

$$\mathrm{J}_0(\sqrt{-\gamma_n}) = 0, \quad n = 1, 2, \ldots. \tag{3.24}$$

Note that $R^{\mathrm{s}}(r)$ is not orthogonal to $R^{\mathrm{c}}(r)$ with respect to r, namely

$$\int_0^1 R^{\mathrm{s}}(r)R^{\mathrm{c}}(r)\,r\,\mathrm{d}r \neq 0. \tag{3.25}$$

The corresponding eigenvalue is

$$\chi_{nl}^{\mathrm{s}} = -l(l+1) - \gamma_n^2, \quad n = 1, 2, \ldots. \tag{3.26}$$

Note that the above sequence of spherical harmonics (3.9), (3.10) and (3.11) with (3.17) and (3.23) is orthonormal with respect to the inner product (3.7). It forms a basis for functions on the local space satisfying the reflective, finite and periodic boundary conditions (2.18)–(2.24). Thus, we call it a 'reflection basis'.

3.2.2. *Galerkin method*

Now we apply the Galerkin method with the above reflection basis to obtain the solution of P_0^∞. We use $\{e_i^{\mathrm{r}}\}_{i=1}^\infty$ to denote the basis; then the expression for P_0^∞ is

$$P_0^\infty(r, \theta, \phi) = \sum_{i=1}^\infty q_i e_i^{\mathrm{r}}(r, \theta, \phi), \tag{3.27}$$

where q_i is the expansion coefficient to be determined. Note that the BVP for P_0^∞ is symmetric with respect to the line $\theta = \pi/2$,

$$P_0^\infty(r, \theta, \phi) = P_0^\infty(r, \pi - \theta, \phi). \tag{3.28}$$

Therefore, only even-symmetric associated Legendre polynomials are used in the expansion, i.e. with $l + m$ even.

To obtain the Galerkin equation, i.e. the weak formulation of (3.5) by inner product with the reflection basis $\{e_i^{\mathrm{r}}\}_{i=1}^\infty$, one needs to construct the bilinear form $a(\cdot, \cdot)$ for the local operator $\mathcal{L}$. In matrix form, the element of the corresponding matrix is

$$A_{ij} = a(e_i^{\mathrm{r}}, e_j^{\mathrm{r}}) = \langle e_i^{\mathrm{r}}, \mathcal{L}e_j^{\mathrm{r}}\rangle, \quad i = 1, 2, \ldots, \ j = 1, 2, \ldots. \tag{3.29}$$

Because P_0^∞ is independent of ψ, equation (3.5) reduces to

$$-Pe_s \sin\theta \sin\phi\,\frac{1}{r}\frac{\partial(rP_0^\infty)}{\partial r} + \nabla_p \cdot (\dot{p}P_0^\infty) = D_t\frac{1}{r}\frac{\partial}{\partial r}\left(r\frac{\partial P_0^\infty}{\partial r}\right) + (\nabla_p \cdot \nabla_p)P_0^\infty. \tag{3.30}$$

The diffusive term (the right-hand side of (3.30)) is Laplacian, and thus it is easy to treat with the reflection basis, resulting in a diagonal matrix for the corresponding bilinear form.

However, the 'convective' term (the left-hand side of (3.30)) is laborious to handle. To simplify the bilinear form with spherical harmonics, recursion relations and identities of associated Legendre polynomials can be imposed (Strand & Kim 1992; Bees, Hill & Pedley 1998; Hill & Bees 2002; Manela & Frankel 2003), but it still leads to lengthy expressions and tedious calculations. We follow Doi & Edwards (1978) and treat the local operator $\mathcal{L}$ in a more systematic way. The angular momentum operators in quantum mechanics are introduced and related to $\mathcal{L}$. Integrals of the spherical harmonics are given by the Wigner 3j-symbols. More details are shown in appendix A. Finally, truncation of the series (3.27) to some degree N gives a Galerkin solution for P_0^∞.

3.3. *Overall drift and dispersivity*

The overall dispersion process in the longitudinal direction can be characterized by the overall drift U_d and dispersivity D_T, which are related to the first- and second-order longitudinal moments of the cross-sectional mean concentration $\langle P \rangle$,

$$U_d \triangleq \lim_{t \to \infty} \frac{\mathrm{d}M_1}{\mathrm{d}t}, \tag{3.31}$$

$$D_T \triangleq \frac{1}{2} \lim_{t \to \infty} \frac{\mathrm{d}}{\mathrm{d}t}(M_2 - M_1^2), \tag{3.32}$$

where M_i is the ith moment of $\langle P \rangle$,

$$M_i \triangleq \int_{-\infty}^{\infty} z^i \langle P \rangle \, \mathrm{d}z, \quad i = 0, 1, 2, \dots. \tag{3.33}$$

Note that the frame of reference is transformed to that moving with the mean flow as shown in (2.11), thus U_d is the drift above the mean flow. Based on the longitudinal moments, one can perform a cumulant expansion for $\langle P \rangle$ and P (Chatwin 1970; Guo *et al.* 2018; Jiang & Chen 2018, 2019*b*), and can include higher-order cumulants like skewness and kurtosis (Frankel & Brenner 1989; Wang & Chen 2017).

According to the GTD theory (Hill & Bees 2002; Jiang & Chen 2019*a*), U_d and D_T can be evaluated as

$$U_d = \langle V_z(r, \theta, \phi) P_0^\infty(r, \theta, \phi) \rangle, \tag{3.34}$$

$$D_T = D_t + \langle V_z(r, \theta, \phi) b(r, \psi, \theta, \phi) \rangle, \tag{3.35}$$

where $V_z(r, \theta, \phi)$ is the total longitudinal speed,

$$V_z(r, \theta, \phi) = Pe_f U(r) + Pe_s p_z(\theta, \phi) = Pe_f U(r) - Pe_s \sin\theta \cos\phi, \tag{3.36}$$

and $b(r, \psi, \theta, \phi)$ is the solution for

$$\mathcal{L}b = P_0^\infty(V_z - U_d), \tag{3.37}$$

with boundary conditions in the same form as those of P_0^∞ (2.18)–(2.24) and the normalization condition

$$\langle b(r, \psi, \theta, \phi) \rangle = 0. \tag{3.38}$$

Parameter	Description	Reference value	Units
V_s^*	Swimming speed	6.3×10^{-5}	m s^{-1}
B^*	Gyrotactic time scale	3.4	s
D_r^*	Rotational diffusivity	0.067	s^{-1}
D_t^*	Translational diffusivity	0	m^2 s^{-1}
a^*	Pipe radius	9.4×10^{-5} to 9.4×10^{-3}	m
U_m^*	Mean flow speed	6.3×10^{-6} to 6.3×10^{-4}	m s^{-1}
λ	Bias parameter	2.2	
α_0	Cell shape factor	0.31	
Pe_s	Swimming Péclet number	0.1–10	
Pe_f	Flow Péclet number	0.01–100	
w_V	Ratio between speeds	0.1–10	

TABLE 1. Dimensional and non-dimensional parameters for dispersion of *C. nivalis* in the present study. The data of cell properties are taken from Pedley & Kessler (1990, 1992) and Hwang & Pedley (2014a).

Like P_0^∞, the above BVP for b is independent of ψ and is symmetric with respect to the line $\theta = \pi/2$. Therefore, one can also apply the Galerkin method with the same reduced reflection basis to obtain the solution for b as

$$b(r, \theta, \phi) = \sum_{i=1}^{\infty} b_i e_i^{\mathrm{r}}(r, \theta, \phi). \tag{3.39}$$

Performing the cross-sectional mean operation (3.34) and (3.35), finally, we obtain the corresponding Galerkin solutions for U_d and D_T.

4. Overall dispersion in Poiseuille flow

We now apply the above one-step GTD theory to the problem of a dilute suspension dispersing in vertical pipe flow. The negative buoyancy of the cells, which can modify the flow (Bees & Croze 2010; Croze *et al.* 2017), is neglected. Thus we consider a Poiseuille flow. For the downwelling case, the speed deviation from the mean is

$$U(r) = 1 - 2r^2, \tag{4.1}$$

and then

$$\frac{\partial U}{\partial r} = -4r. \tag{4.2}$$

We also consider the upwelling case, namely reversing the sign of the velocity and shear, or, equivalently, reversing the sign of λ (the direction of the gyrotactic bias).

The gyrotactic algae, *C. nivalis*, is studied and the results are compared with those of previous studies (Hill & Bees 2002; Bearon *et al.* 2012). The parameters and their reference values used in the present study are listed in table 1. In previous studies (Hill & Bees 2002; Bearon *et al.* 2012), the cell was assumed to be completely spherical ($\alpha_0 = 0$) for simplicity. Here, we test this assumption and consider an ellipsoidal cell ($\alpha_0 = 0.31$). Additionally, a spherical cell in the absence of gyrotactic bias ($\alpha_0 = 0$, $\lambda = 0$) is also considered for comparison.

It is of considerable interest to compare the above results through the one-step GTD method to those produced by the two-step methods, including the GTD and PK models in previous studies (Hill & Bees 2002; Bearon *et al.* 2012). The two-step GTD method requires that the swimming Péclet number Pe_s should be sufficiently small in order to avoid the influence of the reflective boundary (Bearon *et al.* 2011). Additionally, the variation of shear rates relative to swimming should also be small because the convection–diffusion equation for the position space in the first step is approximated by the dispersion of swimming cells in an unbounded homogeneous shear flow. To measure the variation of the shear rates (quantified by $\partial^2(Pe_f U)/\partial r^2 = -4Pe_f$ for the downwelling Poiseuille flow) relative to the swimming term (quantified by Pe_s) in the dimensionless conservation equation (2.13), we introduce the ratio between Péclet numbers,

$$w_V \triangleq \frac{Pe_f}{Pe_s} = \frac{U_m^*}{V_s^*}, \tag{4.3}$$

which is also the ratio of the mean flow speed to the swimming speed. We will show the discrepancy between the results of the one- and two-step methods in the Pe_s–w_V plane.

For the one-step GTD method, the Galerkin method with the reflection basis is applied to obtain the dispersion results. The series expansion is truncated up to $n = 40$ in the radial direction for the gyrotactic focusing and $l = 10$ in the orientation space with spherical harmonics. The resulting Galerkin equation is solved.

For the two-step method, the mathematical structures of the GTD (Hill & Bees 2002; Manela & Frankel 2003) and PK (Pedley & Kessler 1990, 1992) models are summarized by Bearon *et al.* (2012) and Croze *et al.* (2017). The parameters used in the GTD and PK models for *C. nivalis* with $\lambda = 2.2$ can be found in appendix E of Bearon *et al.* (2012). The overall drift and dispersivity are also evaluated by the GTD theory. Detailed calculations are based on Bees & Croze (2010, equations (6.1) and (6.2)); see also Croze *et al.* (2017, equations (2.10) and (2.11)).

4.1. *Local distribution* P_0^∞

The long-time asymptotic state of the zeroth-order moment P_0^∞ is the steady marginal density function in the phase space (r, θ, ϕ) (Ezhilan & Saintillan 2015; Jiang & Chen 2019*a*). As a local distribution, it can demonstrate the gyrotactic focusing and shear alignment of cells.

4.1.1. *Distribution in phase space*

Examples for the gyrotactic focusing of cells in vertical pipe flows are shown in figure 2. For the case of a downwelling flow, cells accumulate near the centre of the tube (Kessler 1984, 1985), with the highest concentration at the centre ($r = 0$). The distributions of cells in the ϕ–θ plane at all the radial positions are similar: cells concentrate near the point $\phi = 0$, $\theta = \pi/2$. Note that there is no obvious swimming bias towards the centre ($0 < \phi < \pi$), which is significantly different from the biased distribution predicted by the FP equation in both the two-step methods (Bearon *et al.* 2011). For the upwelling flow, the results are just reversed: the concentration at the wall ($r = 1$) is the highest (Kessler 1984, 1985).

The structure of the local distribution in the phase space can be captured by the dynamical system theory (Zöttl & Stark 2012, 2013; Santamaria *et al.* 2014). A local
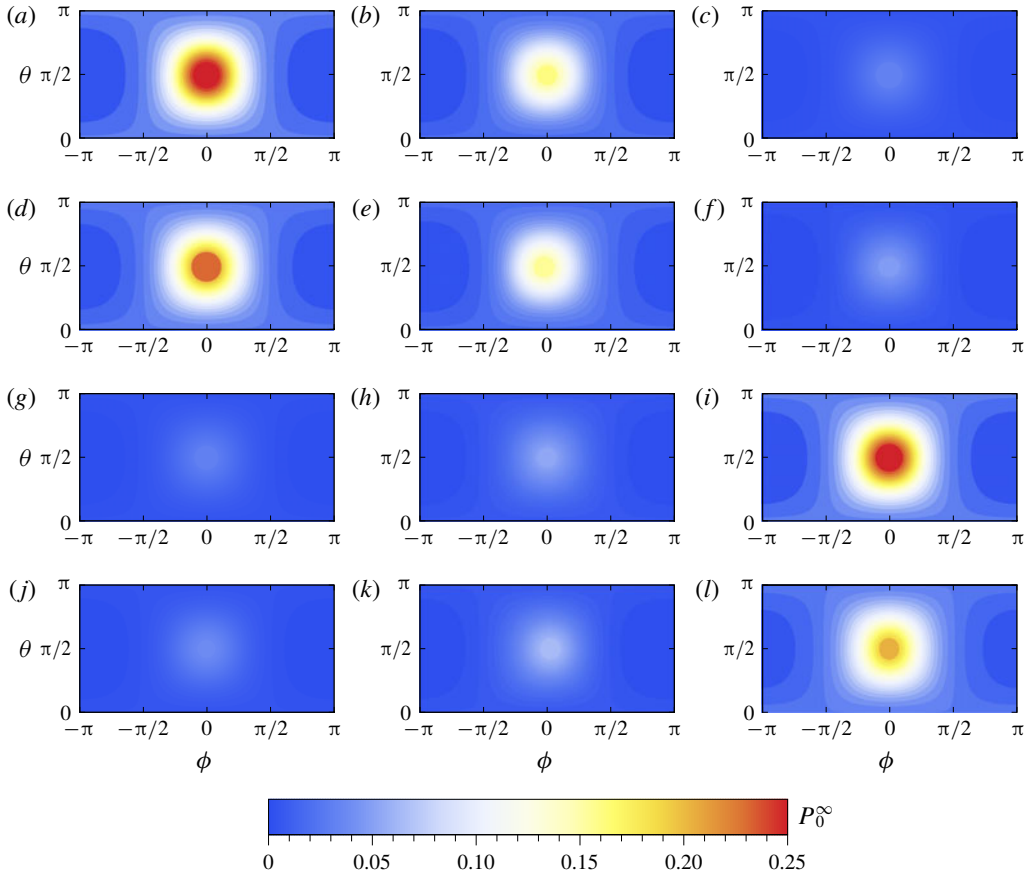
FIGURE 2. Density plot of local distributions $P_0^\infty(r, \theta, \phi)$ of spherical and ellipsoidal gyrotactic cells at different radial positions: (a,d,g,j) $r = 0$; (b,e,h,k) $r = 0.5$; (c,f,i,l) $r = 1$. $(a–c)$ Spheres in downwelling flow $(\alpha_0 = 0)$; $(d–f)$ ellipsoids in downwelling flow $(\alpha_0 = 0.31)$; $(g–i)$ spheres in upwelling flow $(\alpha_0 = 0)$; $(j–l)$ ellipsoids in upwelling flow $(\alpha_0 = 0.31)$. In all cases, $\lambda = 2.2$, $Pe_s = 1$ and $w_V = 1$.

velocity field for the local transport problem in the phase space (r, θ, ϕ) can be defined as (Jiang & Chen 2019*a*)

$$\boldsymbol{u} = (-Pe_s \sin\theta \sin\phi, \dot{\theta}, \dot{\phi}). \tag{4.4}$$

Swimmers will accumulate near stable critical points (with zero local velocity). For vertical downwelling pipe flow, the critical point $(0, \pi/2, 0)$ is stable, where cells swim perfectly upwards, resulting in gyrotactic focusing. In contrast, the critical point $(0, \pi/2, \pi)$ is unstable, where cells swim downwards, resulting in an area with the lowest concentration. For the case of the upwelling flow, the cells accumulate near the reflective boundaries due to swinging motions towards the tube wall, similar to the trapping by tumbling motions near high-shear regions (Zöttl & Stark 2013; Rusconi, Guasto & Stocker 2014). Additionally, for the case of spherical cells without gyrotactic bias $(\alpha_0 = 0, \lambda = 0)$, note that the local velocity field is divergence-free, as shown in § A.2.1. Therefore, the local transport problem (3.30) with reflective

boundary conditions (2.18) and (2.19) has a constant solution $P_0^\infty = 1/(4\pi^2)$. There is no stable critical point and thus no focusing. Note that the incident probability flux at the wall ($r = 1$, $-\pi < \phi < 0$) can be non-zero but is equal to the reflection flux ($0 < \phi < \pi$) because the reflective boundary conditions (2.18) and (2.19) for the continuum transport equation (2.13) are a simplified description of the reflection process, assuming that the incidence and reflection of a cell happen in an instant.

For the influence of cell shape, as shown in figure 2(*a,d*) for the downwelling flow, the main difference between the cases of spheres ($\alpha_0 = 0$) and ellipsoids ($\alpha_0 = 0.31$) is due to the effect of shear alignments. The concentrated area of ellipsoids in figure 2(*d*) is much smaller than that of spheres in figure 2(*a*) because the swimming direction of prolate cells is aligned closely along the streamlines of the flow by the strain effect. However, the focusing of ellipsoids in the radial direction is weaker than that of spheres. Shear alignments reduce the probability that prolate cells can swim towards the centre of the tube, resulting in a more uniform distribution in the radial direction. The discussion for the upwelling case is similar.

4.1.2. *Orientation-space-mean probability density function*

The gyrotactic focusing of cells near the centre of the tube can be illustrated more clearly in terms of the orientation-space-mean p.d.f.

$$\langle P_0^\infty \rangle_O \triangleq \int_0^\pi \sin\theta \, \mathrm{d}\theta \int_0^{2\pi} \mathrm{d}\phi \, P_0^\infty(r, \theta, \phi), \tag{4.5}$$

i.e. the marginal p.d.f. in the position plane r–ψ (here independent of ψ). With the orientation space eliminated, results are compared to those by the two-step models for the transport problem in the position space (Bearon *et al.* 2012).

First, we discuss the case of the downwelling flow. As shown in figure 3, the gyrotactic focusing near the axis of the tube is enhanced with increased flow rates (also quantified by the ratio between speeds w_V with a fixed swimming speed). However, the distributions of the spherical cells in figure 3(*a–c*) are roughly the same. Namely, the focusing of spherical cells is nearly dependent only on w_V, the ratio between the Péclet numbers. Note that the steady gyrotactic focusing can be predicted by a Gaussian distribution (Kessler 1984, 1985; Pedley & Kessler 1992). Near the centre of the tube with sufficiently small shear, Bearon *et al.* (2012) gave an asymptotic solution based on the two-step GTD method, in current notation,

$$\langle P_0^\infty \rangle_O \sim \mathrm{e}^{-\lambda w_V r^2}, \tag{4.6}$$

which depends only on w_V and λ. We remark that this approximate result is hard to obtain directly from the local transport equation (3.30) in the whole phase space by asymptotic analysis, but can be simply derived from the effective transport equation only in the position space by the two-step method; see Bearon *et al.* (2012, equation (24)). In the absence of gyrotactic bias ($\lambda = 0$), there is no focusing and the radial distribution is uniform.

For the influence of cell shape, shear alignments of ellipsoids ($\alpha_0 = 0.31$) can weaken the gyrotactic focusing, which is consistent with previous studies (Bearon *et al.* 2011; Croze *et al.* 2013) for channel flows. Compared with the spherical case ($\alpha_0 = 0$), distributions of ellipsoids are much more uniform in the radial direction. More importantly, the decrease of concentration near the centre of the tube from the spherical case to the ellipsoidal case is greater with both larger flow rates
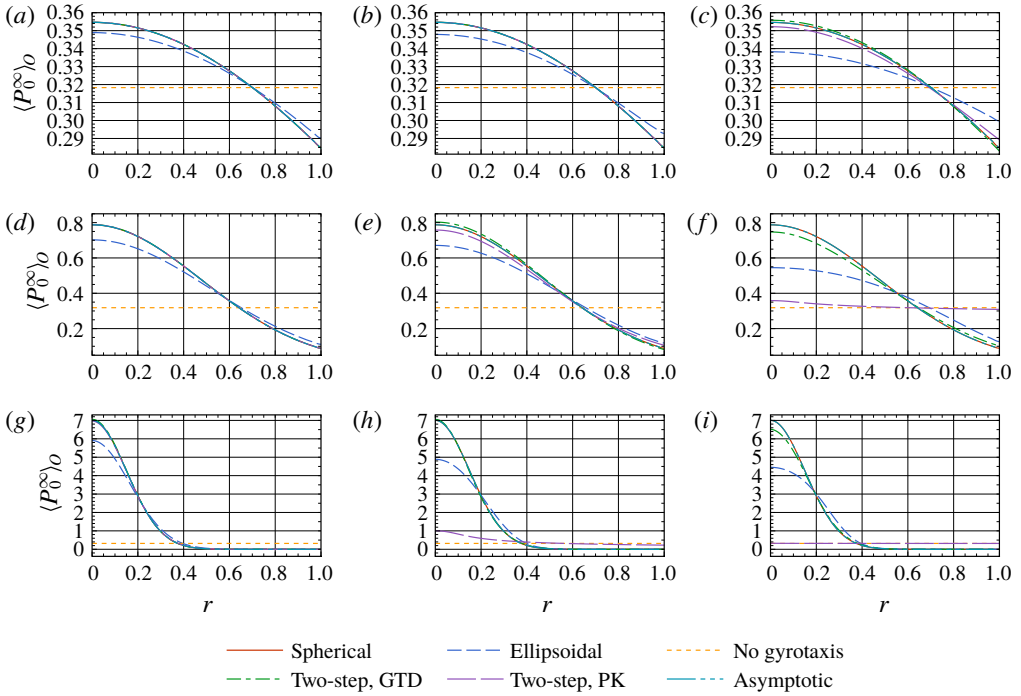
FIGURE 3. Orientation-space-mean p.d.f.s $\langle P_0^\infty \rangle_O$ of cells in the downwelling flow for different swimming Péclet numbers Pe_s: (a,d,g) $Pe_s = 0.1$; (b,e,h) $Pe_s = 1$; (c,f,i) $Pe_s = 10$; and different ratios between speeds w_V: $(a–c)$ $w_V = 0.1$; $(d–f)$ $w_V = 1$; $(g–i)$ $w_V = 10$. 'Spherical' denotes the case of gyrotactic spherical cells ($\alpha_0 = 0$, $\lambda = 2.2$). 'Ellipsoidal' denotes ellipsoidal cells ($\alpha_0 = 0.31$, $\lambda = 2.2$). 'No gyrotaxis' denotes spherical cells without gyrotactic bias ($\alpha_0 = 0$, $\lambda = 0$). 'Two-step, GTD' and 'Two-step, PK' denote the results of spherical cells ($\alpha_0 = 0$, $\lambda = 2.2$) by the two-step method with the GTD and PK models, respectively. 'Asymptotic' denotes the associated asymptotic Gaussian distribution (4.6).

(quantified by w_V) and larger swimming Péclet numbers Pe_s, as shown in figure 3. The reason is that shear alignments by the strain effect can inhibit prolate cells from swimming towards the centre of the tube, as discussed in §4.1.1. The increase of both Pe_s and w_V corresponds to a larger flow Péclet number Pe_f due to the definition of w_V (4.3), as the ratio between the Péclet numbers. Thus, the shear rate and the strain also increase, enhancing the inhibiting effect.

For the case of spherical gyrotactic cells ($\alpha_0 = 0$, $\lambda = 2.2$), both the two-step method with the GTD model and that with the PK model (Bearon *et al.* 2012) give successful predictions with small swimming Péclet numbers Pe_s and relative variations of shear rates of the Poiseuille flow (quantified by w_V). As confirmed in figure 3(*a,b,d*), these three curves are on top of each other. However, outside the required parameter range in the Pe_s–w_V plane, as shown in figure 3(*e,f,h,i*), there are considerable differences of the results by the PK model from the exact results by the one-step method. With stronger shear, more uniform distributions are predicted in the PK model than in GTD models, due to neglecting the local spatial distribution (thus valid only for weak flows) (Bearon *et al.* 2011, 2012; Croze *et al.* 2017). On the other hand, the predictions given by the two-step GTD method are still in agreement
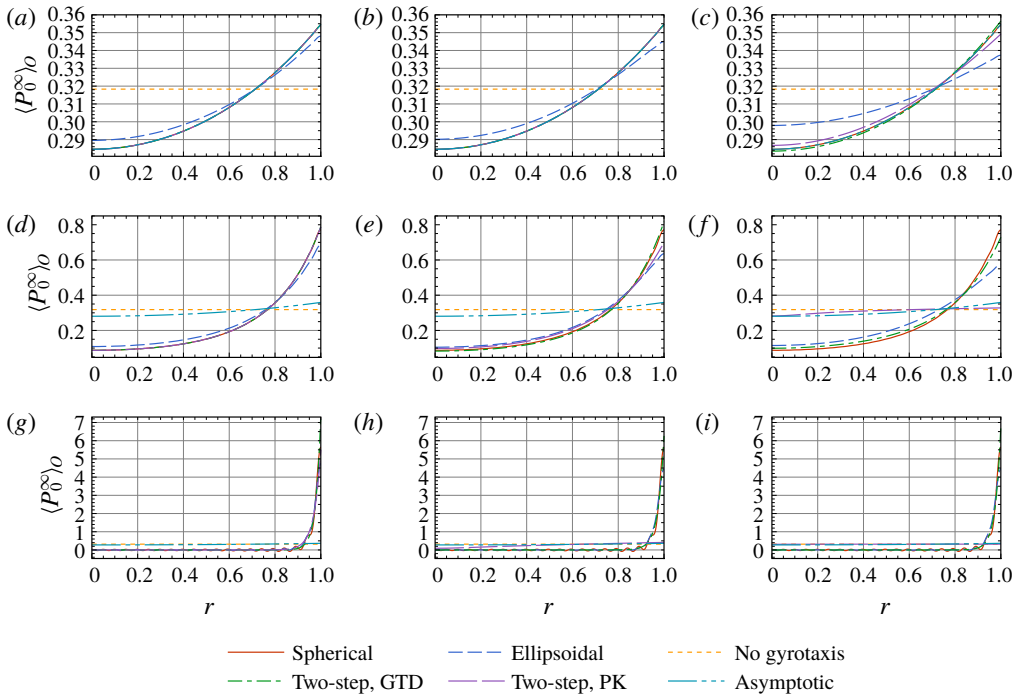
FIGURE 4. Orientation-space-mean p.d.f.s $\langle P_0^\infty \rangle_O$ of cells in the upwelling flow for different swimming Péclet numbers Pe_s: (a,d,g) $Pe_s = 0.1$; (b,e,h) $Pe_s = 1$; (c,f,i) $Pe_s = 10$; and different ratios between speeds w_V: $(a–c)$ $w_V = 0.1$; $(d–f)$ $w_V = 1$; $(g–i)$ $w_V = 10$. 'Spherical' denotes the case of gyrotactic spherical cells ($\alpha_0 = 0$, $\lambda = 2.2$). 'Ellipsoidal' denotes ellipsoidal cells ($\alpha_0 = 0.31$, $\lambda = 2.2$). 'No gyrotaxis' denotes spherical cells without gyrotactic bias ($\alpha_0 = 0$, $\lambda = 0$). 'Two-step, GTD' and 'Two-step, PK' denote the results for spherical cells ($\alpha_0 = 0$, $\lambda = 2.2$) by the two-step method with the GTD and PK models, respectively. 'Asymptotic' denotes the associated asymptotic Gaussian distribution (4.6) with $\lambda = -2.2$.

with the exact results, even in figure 3(i) with large Pe_s and w_V. To some extent, the gyrotactic focusing accumulates cells in the regions with low shear and far from the tube wall, which enlarges the appropriate parameter range for the two-step method (Bearon *et al.* 2011).

Now we turn to the case of the upwelling flow. The distinct difference is that the gyrotactic focusing is near the walls (Kessler 1984, 1985), as shown in figure 4. As in the upwelling case, the orientation-space-mean p.d.f. can still be matched by the asymptotic solution (4.6) with the reversed sign of shear, although the shear near the wall is much larger than that near the centre of the tube. When the shear rate is large, shown in figure 4($g–i$), the focusing is so intense that higher-order basis functions in the radial direction are needed for the series expansion (3.27) to reduce the truncation error. Also, distributions of spherical cells are nearly independent of swimming Péclet number Pe_s with a fixed ratio between speeds w_V, but it is not true for the ellipsoids. The shear alignments can also flatten the distributions in the radial direction. The discussion about the predictions by the two-step methods is analogous: the GTD model gives more successful results than the PK model, even inside the 'breakdown' parameter region.

4.2. *Overall drift and dispersivity for downwelling flow*

For the downwelling flow, the gyrotactic focusing near the centre of the tube, as demonstrated by the local distribution, will exert a strong influence on the overall dispersion process in the longitudinal direction. Results of the overall drift and dispersivity in the parameter plane Pe_s–w_V are presented. Here, we focus on the effects of shear and boundaries on the dispersion coefficients. The influence of cell shape and the predictions by the two-step methods will be tested.

4.2.1. *Influence of shear flow*

First, we discuss the influence of shear on the overall drift of spherical cells. Note that U_d (3.34) is the drift above the mean flow because the frame of reference has been transformed in (2.11). With the swimming Péclet number Pe_s fixed, changing the ratio between speeds w_V in figure 5 corresponds to changing the flow rate and shear rate.

The drift increases monotonically with the flow rate, as shown in figure 5(*a,c,e*). At small flow rates, where the swimming effect is dominant, the drift is negative due to the upward orientation of the cells by the gravitational torque (Bees & Croze 2010; Croze *et al.* 2017). As the flow rate increases, the drift becomes positive because the gyrotactic focusing accumulates cells near the centre of the tube where the flow speed Pe_f is the fastest. Therefore, at high flow rates, it is observed that $U_d \sim Pe_f = w_V Pe_s$, which is consistent with the discussion by Croze *et al.* (2017). In the absence of gyrotactic bias ($\lambda = 0$), there is no drift above the mean flow because the local distribution is uniform in the whole phase space.

Next, for the dispersivity, its variation with flow rate is much more complex. Note that the dispersion process is driven by both the swimming diffusion effect and the convection (Jiang & Chen 2019*a*). When the swimming Péclet number Pe_s is not large, the convection effect plays the central role. As shown in figure 5(*b,d*), the dispersivity rises as the flow rate increases. However, at high flow rates, the dispersivity appears to 'saturate' and then falls with w_V (Croze *et al.* 2013, 2017). The reason is that the gyrotactic focusing of cells near the centre of the tube greatly hinders the effect of convection on the dispersion process. Therefore, without gyrotactic bias ($\lambda = 0$), the dispersivity increases monotonically with the flow rate and is much larger than that of gyrotactic cells.

When the swimming Péclet number Pe_s is large, the strong swimming diffusion drives the macrotransport process. As shown in figure 5(*f*), there are significant differences in the trends of dispersivity with flow rates compared with those in figure 5(*b,d*): the dispersivity will first decrease, then it increases and saturates like the convection-effect-dominated cases. More importantly, in the absence of gyrotaxis, there is also a sharp decrease in dispersivity before the rising. Namely, the imposed shear can reduce the swimming diffusion effect. To find the reason, note that the swimming diffusion effect can be quantified by V_s^2/D_r (Bearon *et al.* 2011). The imposed shear will enhance the rotation of cells, and thus reduce the swimming range, resulting in the decrease of the dispersivity.

Additionally, gyrotaxis can also reduce the swimming diffusion effect. As shown in figure 5(*d,f*) at small flow rates, i.e. the swimming-effect-dominated region, it results in a much smaller dispersivity compared with the no-bias case. Because gyrotaxis forces cells to swim upwards together, the tendency of the cells to separate from each other by swimming with rotation diffusion is weakened. However, the perfectly upward orientation of cells can be disturbed by the imposed shear due to the enhanced rotation, resulting in an increase in dispersivity, in contrast to the
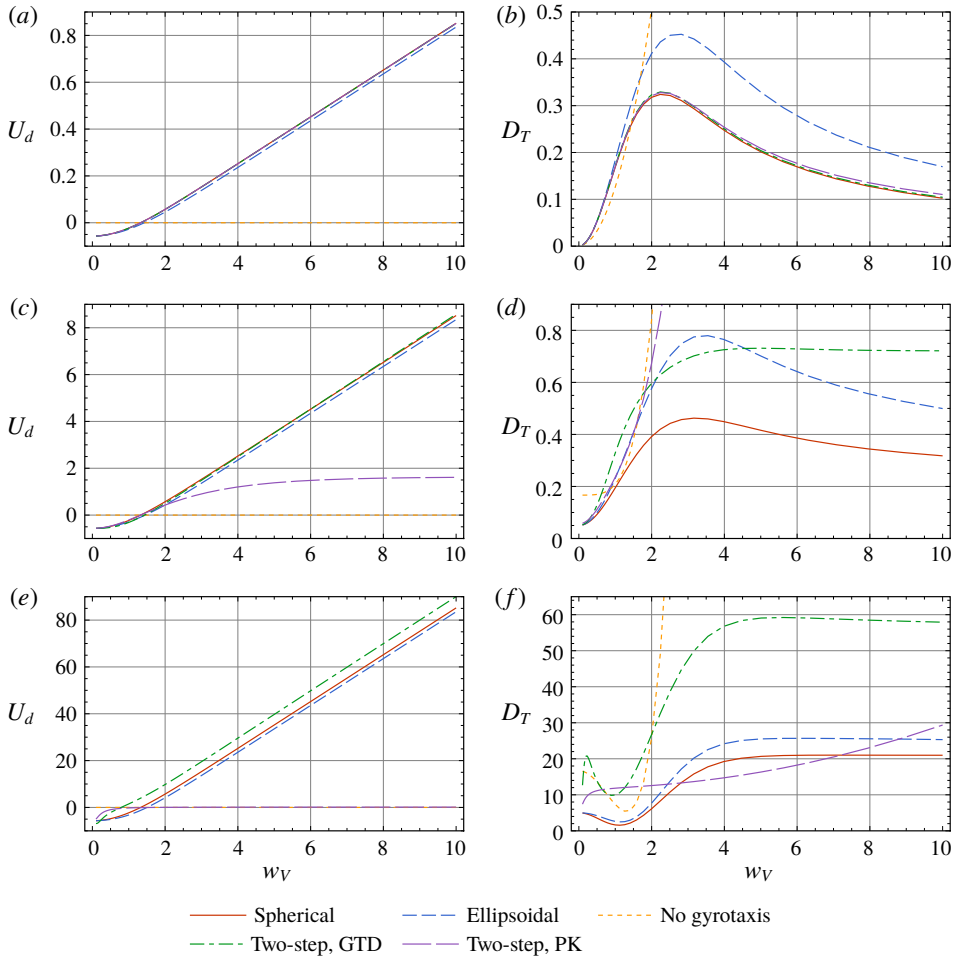
FIGURE 5. For the downwelling flow, variations of (*a,c,e*) overall drift U_d (3.34) and (*b,d,f*) dispersivity D_T (3.35) with the ratio between speeds w_V subject to different fixed swimming Péclet numbers Pe_s: (*a,b*) $Pe_s = 0.1$; (*c,d*) $Pe_s = 1$; (*e,f*) $Pe_s = 10$. 'Spherical' denotes the case of gyrotactic spherical cells ($\alpha_0 = 0$, $\lambda = 2.2$). 'Ellipsoidal' denotes ellipsoidal cells ($\alpha_0 = 0.31$, $\lambda = 2.2$). 'No gyrotaxis' denotes spherical cells without gyrotactic bias ($\alpha_0 = 0$, $\lambda = 0$). 'Two-step, GTD' and 'Two-step, PK' denote the results for spherical cells ($\alpha_0 = 0$, $\lambda = 2.2$) by the two-step method with the GTD and PK models, respectively. Note that with Pe_s fixed, increasing w_V corresponds to increasing the mean speed U_m^*.

decrease discussed above. In fact, these enhanced and reduced effects of the shear rotation on the dispersion process will be balanced: the dispersivity of the gyrotactic case is comparable to that without the bias, as shown in figure 5(*b*) when $w_V < 2$.

With respect to the influence of cell shape, shear alignments of ellipsoids ($\alpha_0 = 0.31$) can slightly reduce the drift and greatly enhance the dispersivity, because the gyrotactic focusing is weakened (Croze *et al.* 2013). As discussed in § 4.1.1, the local distribution of ellipsoids is more uniform in the radial direction, compared with that of spheres. Therefore, more cells swim outside the fast flow zone, decreasing the drift

above the mean flow. Meanwhile, the convection effect on the dispersion process is strengthened.

The predictions by the two-step methods on the dispersion process are compared with the results by the one-step method for the case of spherical gyrotactic cells. When the swimming Péclet number Pe_s is small, as required in the two-step methods, both the GTD and PK models provide perfect results for the drift and dispersivity as expected, also shown in figure 5(*a*,*b*), although there is still a small deviation in dispersivity at high flow rates (quantified by w_V). With larger Pe_s, considerable discrepancies are observed in figure 5(*c*–*f*). Instead of growing with the flow rate, the drift by the PK model tends to be a constant much smaller than the exact one at high flow rates (Croze *et al.* 2013, 2017). As discussed in § 4.1.1, the PK model neglects the local spatial distribution by shear and predicts a more uniform distribution of cells in the radial direction, resulting in a smaller drift similar to the case without gyrotactic bias. In the GTD model, the curve of drift still adheres to the exact one, but curves of dispersivity diverge. The deviation in dispersivity becomes larger as the variation of shear rates in the radial direction (also quantified by the ratio between Péclet numbers w_V for the Poiseuille flow) increases and exceeds the requirements of the first step in obtaining the convection–diffusion equation in the position space.

4.2.2. *Influence of boundaries*

We have tested the predictions produced by the two-step methods on the dispersion process with the variation of shear rates w_V at different swimming Péclet numbers Pe_s. Here, we give a more direct illustration of the influence of Pe_s, with w_V fixed. Note that for *C. nivalis* with fixed swimming velocity V_s^* and rotational diffusivity D_r^*, increasing Pe_s corresponds to decreasing the pipe radius a^*, and thus increasing the influence of boundaries.

Changing Pe_s hardly affects the gyrotactic focusing, as discussed in § 4.1.1. However, it significantly influences the drift and dispersivity as functions of w_V, as shown in figure 5. With a fixed ratio between Péclet numbers w_V, i.e. the relative importance of the shear effect to the swimming effect, increasing Pe_s will enhance both these effects. Therefore, the drift and dispersivity vary monotonically with Pe_s, for both cases of spherical and ellipsoidal cells, as shown in figure 6.

To obtain the convection–diffusion equation in the position space in the two-step methods, a small Pe_s is the key requirement, which means that the influence of boundaries can be neglected (Bearon *et al.* 2011). As shown in figure 6, increasing Pe_s is destructive to the validity of the two-step methods, for both PK and GTD models. The discrepancies in the drift and dispersivity between the two-step methods and the exact ones grow considerably with Pe_s. Note that, although the reflective boundary conditions (2.18) and (2.19) considered in the current study are an idealized condition for the population models, it is demonstrated that the existence of boundaries will lead to significant deviations in the two-step methods. In fact, when boundaries play a central role, more complicated effects, e.g. hydrodynamic interactions between cells and walls (Berke *et al.* 2008), should be taken into consideration in both the one-step and two-step methods for the dispersion process.

4.3. *Overall drift and dispersivity for upwelling flow*

For the upwelling flow, the position of the gyrotactic focusing is reversed from the centre to the wall of the tube. However, the results of the overall drift and dispersivity are similar to those of the downwelling flow. We keep all the parameters the same as
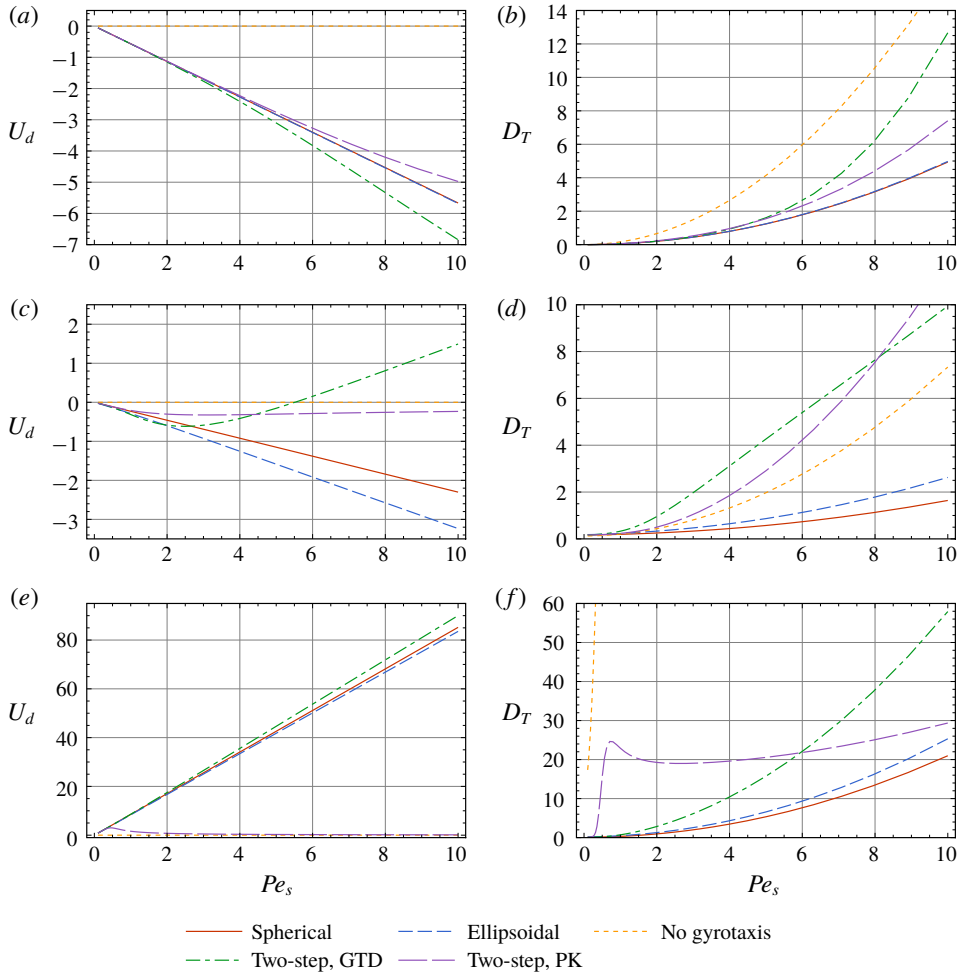
FIGURE 6. For downwelling flow, variations of (a,c,e) overall drift U_d (3.34) and (b,d,f) dispersivity D_T (3.35) with the swimming Péclet number Pe_s subject to different fixed relative variations of shear rates (quantified by the ratio between Péclet numbers w_V): (a,b) $w_V = 0.1$; (c,d) $w_V = 1$; (e,f) $w_V = 10$. 'Spherical' denotes the case of gyrotactic spherical cells ($\alpha_0 = 0$, $\lambda = 2.2$). 'Ellipsoidal' denotes ellipsoidal cells ($\alpha_0 = 0.31$, $\lambda = 2.2$). 'No gyrotaxis' denotes spherical cells without gyrotactic bias ($\alpha_0 = 0$, $\lambda = 0$). 'Two-step, GTD' and 'Two-step, PK' denote the results of spherical cells ($\alpha_0 = 0$, $\lambda = 2.2$) by the two-step method with the GTD and PK models, respectively. Note that for the studied case, increasing Pe_s corresponds to decreasing the pipe radius a^*.

those of the downwelling case and give an analogous discussion on the influence of shear flow.

As in the downwelling case, the drift is monotonic with the flow rate, as shown in figure 7(a,c,e). Note that the drift U_d (3.34) is above the mean flow; thus changing the direction of the flow does not affect the trend of cells towards the mean flow. The explanation for the change of the sign of the drift is similar to those for the downwelling case (Croze *et al.* 2013). At high flow rates, the gyrotactic focusing is
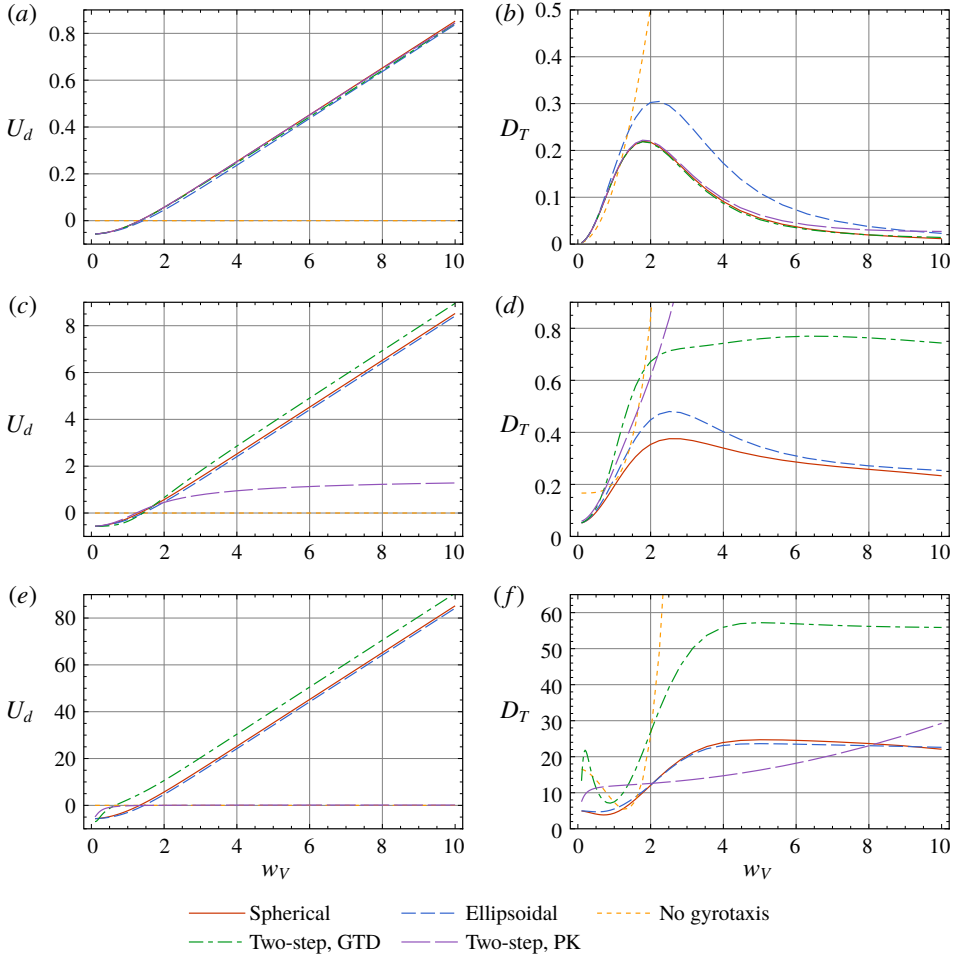
FIGURE 7. For the upwelling flow, variations of (a,c,e) overall drift U_d (3.34) and (b,d,f) dispersivity D_T (3.35) with the ratio between speeds w_V subject to different fixed swimming Péclet numbers Pe_s: (a,b) $Pe_s = 0.1$; (c,d) $Pe_s = 1$; (e,f) $Pe_s = 10$. 'Spherical' denotes the case of gyrotactic spherical cells ($\alpha_0 = 0$, $\lambda = 2.2$). 'Ellipsoidal' denotes ellipsoidal cells ($\alpha_0 = 0.31$, $\lambda = 2.2$). 'No gyrotaxis' denotes spherical cells without gyrotactic bias ($\alpha_0 = 0$, $\lambda = 0$). 'Two-step, GTD' and 'Two-step, PK' denote the results for spherical cells ($\alpha_0 = 0$, $\lambda = 2.2$) by the two-step method with the GTD and PK models, respectively.

near the wall, where the flow rate is also positive to the mean flow, resulting in the positive drift.

For the dispersivity, as shown in figure 7(b,d,f), trends with flow rates are similar to those of the downwelling case: the dispersivity rises and then falls with the ratio between speeds w_V. Also, there is a slight decrease at low flow rates when the swimming Péclet number Pe_s is large. The explanation for gyrotaxis reducing both the convection and the swimming diffusion effects is analogous. However, the changed position of the focusing from the centre to the wall does have an influence on the dispersion process: the dispersivity is significantly smaller, comparing figure 7(b,d)

with figure 5(*b*,*d*). This can be understood by the orientation-space-mean p.d.f.s: the distribution of the upwelling case is not as uniform as the downwelling case. Therefore, the convection effect on the dispersion process is weakened. On the other hand, when the swimming diffusion effect is dominant, as shown in figure 7(*f*) and figure 5(*f*), the dispersivity of the upwelling case is larger. Note that, due to the focusing, the characteristic length for the dispersion process is smaller than the radius of the tube, namely, a larger effective swimming Péclet number can be defined similarly to *Pe*$_s$ as in (2.11). For the upwelling case with a steeper distribution in the radial direction, the effective swimming Péclet number is larger than that of the downwelling case, resulting in the stronger swimming diffusion effect.

For the ellipsoidal swimmers, the influence of shear alignments on the dispersion process is similar to the downwelling case: the drift is reduced and the dispersivity is enhanced, because of the stronger convection effect under a more uniform radial distribution. However, when the swimming diffusion effect is strong, as shown in figure 7(*f*), the dispersivity is comparable to the downwelling one. This is also because of the changed position of the focusing. As discussed above, the swimming diffusion effect is weakened due to the more uniform distribution; thus it cancels out the enhancement by the convection effect.

The predictions by the two-step methods for the upwelling case are also tested. For the overall drift as shown in figure 7(*a*,*c*,*e*), the GTD model gives more successful results than the PK model. However, for the dispersivity, both these two-step methods fail in their 'breakdown' parameter region, as shown in figure 7(*d*,*f*). The reason is similar to the downwelling case: their restrictions on the derivation of the convective–diffusion equation in the position space during the first step. Additionally, the discussion on the influence of boundaries is also similar. As shown in figure 8, the discrepancies in the drift and dispersivity between the two- and one-step methods grow considerably with the swimming Péclet number *Pe*$_s$.

5. Conclusions

For dispersion of dilute suspensions of gyrotactic micro-organisms in vertical pipe flows, previous work used the two-step methods with the PK model and GTD model and obtained only approximate values of the overall drift and dispersivity. This study provides the first analytical derivation for the dispersion coefficients, by the integrated one-step GTD method. Prior to this study, it was difficult to analyse the dispersion process in the 'breakdown' parameter region in the two-step methods due to the restrictive assumptions: both the swimming Péclet number and the variation of shear rates relative to swimming must be sufficiently small. Thus, the results also give a quantitative test for the applicability of the two-step methods, which is of considerable interest.

Another strength of this study is proposing an appropriate function basis under reflective boundary conditions for the series expansion in the Galerkin method. The reflection principle used in previous studies does not apply to the current flow case, because one cannot reflect the pipe flow field on the circular cross-section. Instead, the required basis functions are constructed by cylindrical and spherical harmonics, using the full form of reflective boundary conditions (2.18) and (2.19), including both the probability and its radial derivative. The so-called reflection basis plays the central role in solving the local distribution, the overall drift and the dispersivity in the one-step GTD method.
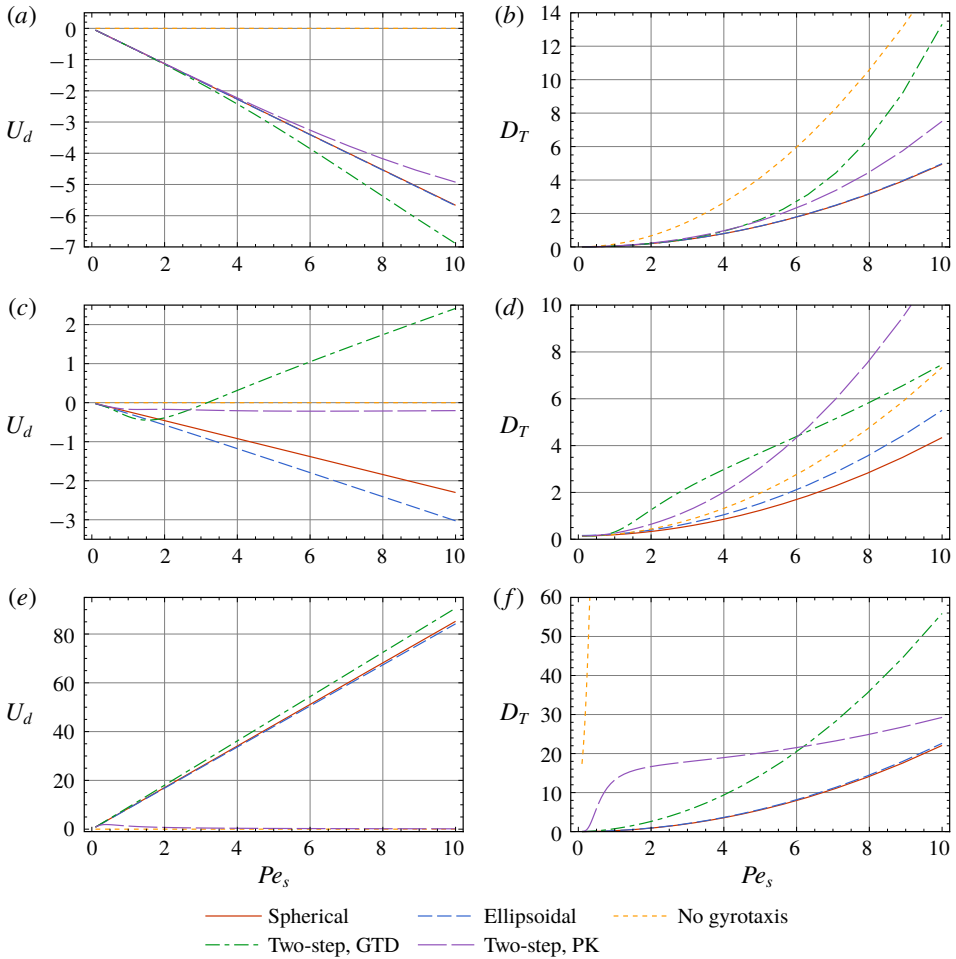
FIGURE 8. For the upwelling flow, variations of (*a,c,e*) overall drift U_d (3.34) and (*b,d,f*) dispersivity D_T (3.35) with the swimming Péclet number Pe_s subject to different fixed relative variations of shear rates (quantified by the ratio between Péclet numbers w_V): (*a,b*) $w_V = 0.1$; (*c,d*) $w_V = 1$; (*e,f*) $w_V = 10$. 'Spherical' denotes the case of gyrotactic spherical cells ($\alpha_0 = 0$, $\lambda = 2.2$). 'Ellipsoidal' denotes ellipsoidal cells ($\alpha_0 = 0.31$, $\lambda = 2.2$). 'No gyrotaxis' denotes spherical cells without gyrotactic bias ($\alpha_0 = 0$, $\lambda = 0$). 'Two-step, GTD' and 'Two-step, PK' denote the results of spherical cells ($\alpha_0 = 0$, $\lambda = 2.2$) by the two-step method with the GTD and PK models, respectively.

Detailed results for *C. nivalis* are presented to illustrate the influence of the gyrotactic focusing on the overall dispersion process, for both the downwelling and upwelling flows. The gyrotactic bias is demonstrated by the local distribution in the phase space. The drift above the mean flow increases monotonically with the flow rate. For the dispersivity, when the flow rate is small, the combined effect of gyrotaxis, swimming and shear on the dispersion process is complicated: the dispersivity first decreases, then increases and finally saturates as the flow rate increases. For prolate cells, shear alignments with streamlines of the imposed flow lead to weaker focusing

than that of spherical ones, and thus reduce the overall drift and greatly enhance the overall dispersivity. For the case of spherical gyrotactic cells, the predictions by the two-step methods are compared with the exact results. Both the PK and GTD models give successful predictions inside their required parameter region. Within the 'breakdown' region, the predictions of the two-step GTD method are still matched for the local distribution and the overall drift, but fail in the overall dispersivity.

This study has only considered dilute suspensions, and idealized reflective boundary conditions are imposed for the theoretical analysis. Future studies should include cell–cell, cell–fluid and cell–wall interactions in the one-step approach for dense suspensions. The challenge is to solve the Smoluchowski equation for transport coupled to the Navier–Stokes equation as modified by adding a new term to reflect the active stress in the flow field (Bees & Croze 2010; Croze *et al.* 2017; Saintillan 2018). Self-organization (Lushi, Wioland & Goldstein 2014) and hydrodynamic instabilities (Pedley & Kessler 1992; Hwang & Pedley 2014*b*) should also be considered in finding the local distribution. Additionally, the dispersion process can be very sensitive to the type of boundary conditions. For example, the Robin boundary condition (Ezhilan & Saintillan 2015) accounting for the wall accumulation effect of micro-organisms like bacteria and sperms can enhance or reduce the overall dispersivity compared with those under the reflective boundary condition (Jiang & Chen 2019*a*). In fact, the experimentally observed behaviour of swimming micro-organisms at boundaries can be much more complicated (Bianchi, Saglimbeni & Di Leonardo 2017; Lushi, Kantsler & Goldstein 2017). Further work is required to develop appropriate boundary conditions for the continuum transport model to characterize the complex cell–wall interactions such as sliding, scattering and steric repulsion effects (Drescher *et al.* 2011; Kantsler *et al.* 2013; Contino *et al.* 2015).

Acknowledgements

Declaration of interests

The authors report no conflict of interest.

Appendix A. Galerkin method with spherical harmonics

The idea of systemically treating spherical harmonics in the Galerkin method was given by Doi & Edwards (1978). The key is to express the local operator $\mathcal{L}$ in terms of the angular momentum operators and multiplication operators with spherical harmonics. Here we reveal their relation generally.

A.1. *Angular momentum operators*

In quantum mechanics, the orbital angular momentum operator is defined as (Doi & Edwards 1978)

$$\boldsymbol{L} \triangleq -\mathrm{i}\hbar(\boldsymbol{r} \times \nabla), \tag{A 1}$$

where $\hbar$ is the Planck constant and $\boldsymbol{r}$ is the position vector. Its three components (L_x, L_y, L_z) in Cartesian coordinates can be expressed in terms of spherical coordinates as

$$L_x = -\mathrm{i}\hbar \left(-\sin\phi \frac{\partial}{\partial\theta} - \cot\theta \cos\phi \frac{\partial}{\partial\phi} \right), \tag{A2}$$

$$L_y = -\mathrm{i}\hbar \left(\cos\phi \frac{\partial}{\partial\theta} - \cot\theta \sin\phi \frac{\partial}{\partial\phi} \right), \tag{A3}$$

$$L_z = -\mathrm{i}\hbar \frac{\partial}{\partial\phi}. \tag{A4}$$

The square of $\boldsymbol{L}$,

$$\boldsymbol{L}^2 = \boldsymbol{L} \cdot \boldsymbol{L} = L_x^2 + L_y^2 + L_z^2, \tag{A5}$$

gives the Laplace operator, and in spherical coordinates

$$\boldsymbol{L}^2 = -\hbar^2 \left[\frac{1}{\sin\theta} \frac{\partial}{\partial\theta} \left(\sin\theta \frac{\partial}{\partial\theta} \right) + \frac{1}{\sin^2\theta} \frac{\partial^2}{\partial\phi^2} \right]. \tag{A6}$$

Note that the results of the angular momentum operator on spherical harmonics are simple. To illustrate, the spherical harmonics (3.9), (3.10) and (3.11) are redefined with complex exponentials

$$\mathrm{Y}_l^m(\theta, \phi) = \sqrt{\frac{2l+1}{4\pi} \frac{(l-m)!}{(l+m)!}} \, \mathrm{P}_l^m(\cos\theta) \mathrm{e}^{\mathrm{i}m\phi}, \tag{A7}$$

where $m = -l, -(l-1), \ldots, 0, \ldots, l-1$. The orthogonality relationship is

$$\int_0^{2\pi} \mathrm{d}\phi \int_0^{\pi} \overline{\mathrm{Y}_{l'}^{m'}}(\theta, \phi) \mathrm{Y}_l^m(\theta, \phi) \sin\theta \, \mathrm{d}\theta = \delta_{ll'} \delta_{mm'}, \tag{A8}$$

where the bar denotes the complex conjugate. For L_z on spherical harmonics,

$$L_z \mathrm{Y}_l^m(\theta, \phi) = m\hbar \mathrm{Y}_l^m(\theta, \phi). \tag{A9}$$

For components L_x and L_y, one can introduce the ladder operators (Doi & Edwards 1978)

$$L_{\pm} \triangleq L_x \pm \mathrm{i}L_y, \tag{A10}$$

which have the following important property:

$$L_{\pm} \mathrm{Y}_l^m(\theta, \phi) = \hbar [l(l+1) - m(m \pm 1)]^{1/2} \mathrm{Y}_l^{m\pm 1}(\theta, \phi). \tag{A11}$$

Therefore, one can use

$$L_x = \tfrac{1}{2}(L_+ + L_-), \tag{A12}$$

$$L_y = -\mathrm{i}\tfrac{1}{2}(L_+ - L_-), \tag{A13}$$

to obtain the results of their action on spherical harmonics.

A.2. *Expression of local operator by angular momentum operators*

In the swimming orientation space, the local operator $\mathcal{L}$ can be expressed in terms of the angular momentum operator $\boldsymbol{L}$. The main part of $\mathcal{L}$ (3.2) that needs treating is

$$\mathcal{L}_p f \triangleq \boldsymbol{\nabla}_p \cdot (\dot{\boldsymbol{p}}_r f), \tag{A 14}$$

because

$$\boldsymbol{\nabla}_p \cdot \boldsymbol{\nabla}_p = \Delta_p = -\frac{\boldsymbol{L}^2}{\hbar^2} \tag{A 15}$$

is just the Laplace operator in the orientation space and the radial convective term in (3.30) can be written as

$$\begin{aligned}
- Pe_s \sin\theta \sin\phi \frac{1}{r}\frac{\partial (rf)}{\partial r} &= -Pe_s \sin\theta \sin\phi \left(\frac{f}{r} + \frac{\partial f}{\partial r}\right) \\
&= -Pe_s \mathrm{i}\sqrt{\frac{2\pi}{3}}[\mathrm{Y}_1^{-1}(\theta, \varphi) + \mathrm{Y}_1^1(\theta, \varphi)]\left(\frac{f}{r} + \frac{\partial f}{\partial r}\right). \tag{A 16}
\end{aligned}$$

Note that according to (2.4) and (2.14), $\mathcal{L}_p$ (A 14) can be rewritten as

$$\mathcal{L}_p f = \boldsymbol{\nabla}_p \cdot \left[(\boldsymbol{\Omega}_r \times \boldsymbol{p})f\right], \tag{A 17}$$

where $\boldsymbol{\Omega}_r$ is the dimensionless relative angular velocity,

$$\begin{aligned}
\boldsymbol{\Omega}_r &= \boldsymbol{\Omega}_a - \dot{\psi}\boldsymbol{e}_z \\
&= \lambda\boldsymbol{p} \times \boldsymbol{k} + \frac{1}{2}Pe_f\boldsymbol{\omega} + \alpha_0 Pe_f[\boldsymbol{p} \times (\boldsymbol{E} \cdot \boldsymbol{p})] - \frac{Pe_s \cos\theta}{r}\boldsymbol{e}_z, \tag{A 18}
\end{aligned}$$

and the dimensionless total angular velocity is $\boldsymbol{\Omega}_a \triangleq \boldsymbol{\Omega}_a^*/D_r^*$.

Next is to pass $\mathcal{L}_p$ to the whole spherical coordinate system, i.e. the whole momentum space with the employed spherical coordinates (ρ, θ, ϕ). At each point (r, ψ, z) of the position space, we also employ a Cartesian coordinate system for the momentum space, with $\hat{\boldsymbol{x}} = -\boldsymbol{e}_z$, $\hat{\boldsymbol{y}} = -\boldsymbol{e}_r$ and $\hat{\boldsymbol{z}} = \boldsymbol{e}_\psi$. To distinguish the gradient operator for the momentum space from $\boldsymbol{\nabla}_p$ on the unit sphere (orientation space), we use $\boldsymbol{\nabla}_s$ to denote it. Now the angular momentum operator (A 1) can be introduced to the momentum space as

$$\begin{aligned}
\boldsymbol{L} &= -\mathrm{i}\hbar(\boldsymbol{\rho} \times \boldsymbol{\nabla}_s) \\
&= L_x\hat{\boldsymbol{x}} + L_y\hat{\boldsymbol{y}} + L_z\hat{\boldsymbol{z}} \\
&= -L_x\boldsymbol{e}_z - L_y\boldsymbol{e}_r + L_z\boldsymbol{e}_\psi, \tag{A 19}
\end{aligned}$$

where $\boldsymbol{\rho} = \rho\boldsymbol{e}_\rho = \rho\boldsymbol{p}$ is the 'position' vector in the momentum space.

Note that operator $\mathcal{L}_p$ (A 17) is independent of ρ. Therefore, its results on the unit sphere ($\rho = 1$) in the momentum space are the same as those in the original orientation space:

$$\begin{aligned}
\mathcal{L}_p f &= \boldsymbol{\nabla}_s \cdot (\boldsymbol{\Omega}_r \times \boldsymbol{p}f) \\
&= (\boldsymbol{\nabla}_s \times \boldsymbol{\Omega}_r) \cdot \boldsymbol{p}f - \boldsymbol{\Omega}_r \cdot [\boldsymbol{\nabla}_s \times (\boldsymbol{p}f)]. \tag{A 20}
\end{aligned}$$

With $\nabla_s \times \boldsymbol{p} = 0$, the second term of (A 20) can be expressed by the angular momentum operator (A 19)

$$
\begin{aligned}
\nabla_s \times (\boldsymbol{p}f) &= -\boldsymbol{p} \times \nabla_s f + (\nabla_s \times \boldsymbol{p})f \\
&= \frac{\boldsymbol{L}}{i\hbar\rho}f \\
&= \frac{\boldsymbol{L}}{i\hbar}f.
\end{aligned}
\tag{A 21}
$$

Finally,

$$
\mathcal{L}_p f = (\nabla_s \times \boldsymbol{\Omega}_r) \cdot \boldsymbol{p}f - \left(\boldsymbol{\Omega}_r \cdot \frac{\boldsymbol{L}}{i\hbar}\right)f.
\tag{A 22}
$$

Note that this form of $\mathcal{L}_p$ can also be obtained using the rotation operator (Brenner & Condiff 1972).

A.2.1. *Detailed expression for $\mathcal{L}_p$*

We substitute $\boldsymbol{\Omega}_r$ (A 18) into (A 22) to obtain the detailed expression for $\mathcal{L}_p$. The coefficients of $\mathcal{L}_p$ are replaced with corresponding spherical harmonics as multipliers for the bilinear form. In matrix form, the dimensionless relative angular velocity is

$$
\begin{aligned}
\boldsymbol{\Omega}_r &= \lambda \begin{pmatrix} -\cos\theta \\ -\sin\theta\sin\phi \\ 0 \end{pmatrix} + \frac{Pe_f}{2}\frac{\partial U}{\partial r}\begin{pmatrix} 0 \\ -1 \\ 0 \end{pmatrix} \\
&\quad + \frac{\alpha_0 Pe_f}{2}\frac{\partial U}{\partial r}\begin{pmatrix} -\cos\theta\sin\theta\sin\phi \\ \sin^2\theta\cos2\phi \\ \cos\theta\sin\theta\cos\phi \end{pmatrix} - \frac{Pe_s\cos\theta}{r}\begin{pmatrix} 0 \\ 0 \\ 1 \end{pmatrix} \\
&= \lambda \begin{pmatrix} -2\sqrt{\dfrac{\pi}{3}}Y_1^0 \\ -i\sqrt{\dfrac{2\pi}{3}}(Y_1^1 + Y_1^{-1}) \\ 0 \end{pmatrix} + \frac{Pe_f}{2}\frac{\partial U}{\partial r}\begin{pmatrix} 0 \\ -1 \\ 0 \end{pmatrix} \\
&\quad + \frac{\alpha_0 Pe_f}{2}\frac{\partial U}{\partial r}\begin{pmatrix} -i\sqrt{\dfrac{2\pi}{15}}(Y_2^1 + Y_2^{-1}) \\ 2\sqrt{\dfrac{2\pi}{15}}(Y_2^2 + Y_2^{-2}) \\ \sqrt{\dfrac{2\pi}{15}}(-Y_2^1 + Y_2^{-1}) \end{pmatrix} - \frac{Pe_s}{r}2\sqrt{\dfrac{\pi}{3}}Y_1^0\begin{pmatrix} 0 \\ 0 \\ 1 \end{pmatrix}.
\end{aligned}
\tag{A 23}
$$

The divergence term $(\nabla_s \times \boldsymbol{\Omega}_r) \cdot \boldsymbol{p}$ in $\mathcal{L}_p$ (A 22) can be further simplified. For the gyrotactic term of $\boldsymbol{\Omega}_r$, one has

$$
\begin{aligned}
\lambda[\nabla_s \times (\boldsymbol{p} \times \boldsymbol{k})] \cdot \boldsymbol{p} &= -\lambda\boldsymbol{p} \cdot [(\boldsymbol{k} \cdot \nabla_s)\boldsymbol{p} + \boldsymbol{k}(\nabla_s \cdot \boldsymbol{p})] \\
&= -\lambda\left[\frac{1}{2}\boldsymbol{k} \cdot \nabla(\boldsymbol{p} \cdot \boldsymbol{p}) + \frac{2}{\rho}\boldsymbol{p} \cdot \boldsymbol{k}\right] \\
&= -2\lambda\boldsymbol{p} \cdot \boldsymbol{k}
\end{aligned}
$$

$$= -2\lambda \sin \theta \cos \phi$$

$$= -2\lambda \sqrt{\frac{2\pi}{3}} [Y_1^{-1}(\theta, \varphi) - Y_1^1(\theta, \varphi)]. \quad (A\,24)$$

For the vorticity term of $\boldsymbol{\Omega}_r$,

$$[\nabla_s \times (\tfrac{1}{2} Pe_f \boldsymbol{\omega})] \cdot \boldsymbol{p} = 0. \quad (A\,25)$$

For the strain-tensor term of $\boldsymbol{\Omega}_r$,

$$\boldsymbol{p} \cdot \{\nabla_s \times [\boldsymbol{p} \times (\boldsymbol{E} \cdot \boldsymbol{p})]\}$$
$$= \boldsymbol{p} \cdot \{[(\boldsymbol{E} \cdot \boldsymbol{p}) \cdot \nabla_s]\boldsymbol{p} - \boldsymbol{p} \cdot \nabla_s(\boldsymbol{E} \cdot \boldsymbol{p}) + \boldsymbol{p} \operatorname{div}(\boldsymbol{E} \cdot \boldsymbol{p}) - (\boldsymbol{E} \cdot \boldsymbol{p}) \operatorname{div} \boldsymbol{p}\}$$
$$= \frac{1}{2}\boldsymbol{p} \cdot \boldsymbol{E} \cdot \nabla_s(\boldsymbol{p} \cdot \boldsymbol{p}) - \boldsymbol{p} \cdot \boldsymbol{E} \cdot [\nabla_s(\boldsymbol{p} \cdot \boldsymbol{p})] + \boldsymbol{E} : \nabla_s \boldsymbol{p} - \boldsymbol{p} \cdot \boldsymbol{E} \cdot \boldsymbol{p}\frac{2}{\rho}$$
$$= \boldsymbol{E} : \nabla_s \boldsymbol{p} - \boldsymbol{p} \cdot \boldsymbol{E} \cdot \boldsymbol{p}\frac{2}{\rho}$$
$$= \boldsymbol{E} : \left(-\frac{1}{\rho}\boldsymbol{p}\boldsymbol{p} + \frac{1}{\rho}\boldsymbol{I}\right) - \boldsymbol{p} \cdot \boldsymbol{E} \cdot \boldsymbol{p}\frac{2}{\rho}$$
$$= \operatorname{tr}(\boldsymbol{E}) - 3\boldsymbol{p} \cdot \boldsymbol{E} \cdot \boldsymbol{p}, \quad (A\,26)$$

where tr denotes the trace and the following identity

$$\nabla_s \boldsymbol{p} = \nabla_s \left(\frac{1}{\rho}\boldsymbol{\rho}\right) = \nabla_s \left(\frac{1}{\rho}\right)\boldsymbol{\rho} + \frac{1}{\rho}\nabla_s \boldsymbol{\rho}$$
$$= -\frac{1}{\rho^3}\boldsymbol{\rho}\boldsymbol{\rho} + \frac{1}{\rho}\boldsymbol{I}$$
$$= -\frac{1}{\rho}\boldsymbol{p}\boldsymbol{p} + \frac{1}{\rho}\boldsymbol{I} \quad (A\,27)$$

is used. Let $\rho = 1$, then

$$\alpha_0 Pe_f \boldsymbol{p} \cdot \{\nabla_s \times [\boldsymbol{p} \times (\boldsymbol{E} \cdot \boldsymbol{p})]\} = -\frac{3}{2}\alpha_0 Pe_f \frac{\partial U}{\partial r} \sin^2 \theta \sin 2\phi$$
$$= -\mathrm{i}3\alpha_0 Pe_f \frac{\partial U}{\partial r} \sqrt{\frac{2\pi}{15}}(Y_2^{-2} - Y_2^2). \quad (A\,28)$$

For the Coriolis term of $\boldsymbol{\Omega}_r$,

$$\boldsymbol{p} \cdot \left[\nabla_s \times \left(-\frac{Pe_s \cos \theta}{r}\boldsymbol{e}_z\right)\right] = -\frac{Pe_s}{r}\boldsymbol{p} \cdot \{\nabla_s \times [(\boldsymbol{e}_\psi \cdot \boldsymbol{p})\boldsymbol{e}_z]\}$$
$$= -\frac{Pe_s}{r}\boldsymbol{p} \cdot [\nabla_s(\boldsymbol{e}_\psi \cdot \boldsymbol{p}) \times \boldsymbol{e}_z]$$
$$= -\frac{Pe_s}{r}\boldsymbol{p} \cdot [(\boldsymbol{e}_\psi \cdot \nabla_s \boldsymbol{p}) \times \boldsymbol{e}_z]$$
$$= -\frac{Pe_s}{r}\boldsymbol{p} \cdot (\boldsymbol{e}_\psi \times \boldsymbol{e}_z)$$
$$= -\frac{Pe_s}{r}\boldsymbol{p} \cdot \boldsymbol{e}_r, \quad (A\,29)$$

which cancels out the radial divergence $-Pe_s \sin \theta \sin \phi \, (1/r)$ in the radial convective term of (A 16).

A.3. *Bilinear form for Galerkin equation*

Note that the coefficients of $\mathcal{L}$ have been replaced with corresponding spherical harmonics; thus one can use the Wigner 3j-symbols to construct the matrix for the bilinear form for the Galerkin equation (Doi & Edwards 1978; Messiah 2014; Nambiar *et al.* 2019).

The coefficients are treated as multiplication operators with multipliers like Y_p^q. For the bilinear form with the complex spherical harmonics,

$$
\begin{aligned}
\int_0^{2\pi} \int_0^\pi \overline{Y_{l'}^{m'}} Y_p^q Y_l^m \sin\theta \, \mathrm{d}\theta \, \mathrm{d}\phi &= \int_0^{2\pi} \int_0^\pi (-1)^{m'} Y_{l'}^{-m'} Y_p^q Y_l^m \sin\theta \, \mathrm{d}\theta \, \mathrm{d}\phi \\
&= (-1)^{m'} \sqrt{\frac{(2l'+1)(2p+1)(2l+1)}{4\pi}} \\
&\quad \times \begin{pmatrix} l' & p & l \\ 0 & 0 & 0 \end{pmatrix} \begin{pmatrix} l' & p & l \\ -m' & q & m \end{pmatrix},
\end{aligned} \tag{A 30}
$$

where the conjugation $\overline{Y_l^m} = (-1)^m Y_l^{-m}$. Note that with the selection rules of the Wigner 3j-symbols (Messiah 2014), only several elements are not zero (Doi & Edwards 1978). Additionally, all the multiplication operators in $\mathcal{L}$ are Hermitian because P_0^∞ is a real function.

To obtain the matrix for the bilinear form with the reflection basis (3.9), (3.10) and (3.11), a change of bases from complex spherical harmonics to their real parts is needed. The transformation is

$$
\sqrt{2}\sqrt{\frac{2l+1}{4\pi}\frac{(l-m)!}{(l+m)!}}\cos(m\phi)P_l^m(\cos\theta) = \frac{\sqrt{2}}{2}[Y_l^m(\theta,\phi) + (-1)^m Y_l^{-m}(\theta,\phi)], \tag{A 31}
$$

$$
\sqrt{2}\sqrt{\frac{2l+1}{4\pi}\frac{(l-m)!}{(l+m)!}}\sin(m\phi)P_l^m(\cos\theta) = -\frac{\sqrt{2}}{2}\mathrm{i}[Y_l^m(\theta,\phi) - (-1)^m Y_l^{-m}(\theta,\phi)], \tag{A 32}
$$

for $m \neq 0$. The corresponding transformation matrix is unitary. Then one can perform a congruent transformation with respect to the conjugate transpose to obtain the bilinear form under the reflection basis.

REFERENCES

ACIÉN, F. G., MOLINA, E., REIS, A., TORZILLO, G., ZITTELLI, G. C., SEPÚLVEDA, C. & MASOJÍDEK, J. 2017 Photobioreactors for the production of microalgae. In *Microalgae-Based Biofuels and Bioproducts* (ed. C. Gonzalez-Fernandez & R. Muñoz), pp. 1–44. Woodhead Publishing.

ARIS, R. 1956 On the dispersion of a solute in a fluid flowing through a tube. *Proc. R. Soc. Lond.* A **235** (1200), 67–77.

BEARON, R. N., BEES, M. A. & CROZE, O. A. 2012 Biased swimming cells do not disperse in pipes as tracers: a population model based on microscale behaviour. *Phys. Fluids* **24** (12), 121902.

BEARON, R. N., HAZEL, A. L. & THORN, G. J. 2011 The spatial distribution of gyrotactic swimming micro-organisms in laminar flow fields. *J. Fluid Mech.* **680**, 602–635.

BEES, M. A. & CROZE, O. A. 2010 Dispersion of biased swimming micro-organisms in a fluid flowing through a tube. *Proc. R. Soc. Lond.* A **466** (2119), 2057–2077.

BEES, M. A. & CROZE, O. A. 2014 Mathematics for streamlined biofuel production from unicellular algae. *Biofuels* **5** (1), 53–65.

BEES, M. A., HILL, N. A. & PEDLEY, T. J. 1998 Analytical approximations for the orientation distribution of small dipolar particles in steady shear flows. *J. Math. Biol.* **36** (3), 269–298.

BERKE, A. P., TURNER, L., BERG, H. C. & LAUGA, E. 2008 Hydrodynamic attraction of swimming microorganisms by surfaces. *Phys. Rev. Lett.* **101** (3), 038102.

BIANCHI, S., SAGLIMBENI, F. & DI LEONARDO, R. 2017 Holographic imaging reveals the mechanism of wall entrapment in swimming bacteria. *Phys. Rev.* X **7** (1), 011010.

BRENNER, H. 1982 A general theory of Taylor dispersion phenomena. II. An extension. *Physico-Chem. Hydrodyn.* **3** (2), 139–157.

BRENNER, H. & CONDIFF, D. W. 1972 Transport mechanics in systems of orientable particles. III. Arbitrary particles. *J. Colloid Interface Sci.* **41** (2), 228–274.

CENCINI, M., BOFFETTA, G., BORGNINO, M. & DE LILLO, F. 2019 Gyrotactic phytoplankton in laminar and turbulent flows: a dynamical systems approach. *Eur. Phys. J.* E **42** (3), 31.

CHATWIN, P. C. 1970 The approach to normality of the concentration distribution of a solute in a solvent flowing along a straight pipe. *J. Fluid Mech.* **43** (2), 321–352.

CHILDRESS, S., LEVANDOWSKY, M. & SPIEGEL, E. A. 1975 Pattern formation in a suspension of swimming microorganisms: equations and stability theory. *J. Fluid Mech.* **69** (3), 591–613.

CHISTI, Y. 2007 Biodiesel from microalgae. *Biotechnol. Adv.* **25** (3), 294–306.

CONTINO, M., LUSHI, E., TUVAL, I., KANTSLER, V. & POLIN, M. 2015 Microalgae scatter off solid surfaces by hydrodynamic and contact forces. *Phys. Rev. Lett.* **115** (25), 258102.

CROZE, O. A., BEARON, R. N. & BEES, M. A. 2017 Gyrotactic swimmer dispersion in pipe flow: testing the theory. *J. Fluid Mech.* **816**, 481–506.

CROZE, O. A., SARDINA, G., AHMED, M., BEES, M. A. & BRANDT, L. 2013 Dispersion of swimming algae in laminar and turbulent channel flows: consequences for photobioreactors. *J. R. Soc. Interface* **10** (81), 20121041.

DOI, M. & EDWARDS, S. F. 1978 Dynamics of rod-like macromolecules in concentrated solution. Part 2. *J. Chem. Soc. Faraday Trans.* **74**, 918–932.

DOI, M. & EDWARDS, S. F. 1988 Brownian motion. In *The Theory of Polymer Dynamics*, pp. 46–90. Oxford University Press.

DRESCHER, K., DUNKEL, J., CISNEROS, L. H., GANGULY, S. & GOLDSTEIN, R. E. 2011 Fluid dynamics and noise in bacterial cell–cell and cell–surface scattering. *Proc. Natl Acad. Sci. USA* **108** (27), 10940–10945.

DURHAM, W. M., KESSLER, J. O. & STOCKER, R. 2009 Disruption of vertical motility by shear triggers formation of thin phytoplankton layers. *Science* **323** (5917), 1067–1070.

DURHAM, W. M. & STOCKER, R. 2012 Thin phytoplankton layers: characteristics, mechanisms, and consequences. *Annu. Rev. Mar. Sci.* **4** (1), 177–207.

ELGETI, J. & GOMPPER, G. 2013 Wall accumulation of self-propelled spheres. *Eur. Phys. Lett.* **101** (4), 48003.

EZHILAN, B., PAHLAVAN, A. A. & SAINTILLAN, D. 2012 Chaotic dynamics and oxygen transport in thin films of aerotactic bacteria. *Phys. Fluids* **24** (9), 091701.

EZHILAN, B. & SAINTILLAN, D. 2015 Transport of a dilute active suspension in pressure-driven channel flow. *J. Fluid Mech.* **777**, 482–522.

FENCHEL, T. & FINLAY, B. J. 1984 Geotaxis in the ciliated protozoon *Loxodes*. *J. Expl Biol.* **110** (1), 17–33.

FENCHEL, T. & FINLAY, B. J. 1986 Photobehavior of the ciliated protozoon *Loxodes*: taxic, transient, and kinetic responses in the presence and absence of oxygen. *J. Protozool.* **33** (2), 139–145.

FRANKEL, I. & BRENNER, H. 1989 On the foundations of generalized Taylor dispersion theory. *J. Fluid Mech.* **204**, 97–119.

FRANKEL, I. & BRENNER, H. 1991 Generalized Taylor dispersion phenomena in unbounded homogeneous shear flows. *J. Fluid Mech.* **230**, 147–181.

FRANKEL, I. & BRENNER, H. 1993 Taylor dispersion of orientable Brownian particles in unbounded homogeneous shear flows. *J. Fluid Mech.* **255**, 129–156.

GARCIA, X., RAFAÏ, S. & PEYLA, P. 2013 Light control of the flow of phototactic microswimmer suspensions. *Phys. Rev. Lett.* **110** (13), 138106.

GOLDSTEIN, R. E. 2015 Green algae as model organisms for biological fluid dynamics. *Annu. Rev. Fluid Mech.* **47** (1), 343–375.

GUO, J., WU, X., JIANG, W. & CHEN, G. 2018 Contaminant transport from point source on water surface in open channel flow with bed absorption. *J. Hydrol.* **561**, 295–303.

HILL, J., KALKANCI, O., McMURRY, J. L. & KOSER, H. 2007 Hydrodynamic surface interactions enable *E. coli* to seek efficient routes to swim upstream. *Phys. Rev. Lett.* **98** (6), 068101.

HILL, N. A. & BEES, M. A. 2002 Taylor dispersion of gyrotactic swimming micro-organisms in a linear flow. *Phys. Fluids* **14** (8), 2598–2605.

HWANG, Y. & PEDLEY, T. J. 2014a Bioconvection under uniform shear: linear stability analysis. *J. Fluid Mech.* **738**, 522–562.

HWANG, Y. & PEDLEY, T. J. 2014b Stability of downflowing gyrotactic microorganism suspensions in a two-dimensional vertical channel. *J. Fluid Mech.* **749**, 750–777.

ISHIKAWA, T. 2012 Vertical dispersion of model microorganisms in horizontal shear flow. *J. Fluid Mech.* **705**, 98–119.

ISHIKAWA, T. & PEDLEY, T. J. 2007 Diffusion of swimming model micro-organisms in a semi-dilute suspension. *J. Fluid Mech.* **588**, 437–462.

ISHIKAWA, T. & PEDLEY, T. J. 2008 Coherent structures in monolayers of swimming particles. *Phys. Rev. Lett.* **100** (8), 088103.

JAKUSZEIT, T., CROZE, O. A. & BELL, S. 2019 Diffusion of active particles in a complex environment: role of surface scattering. *Phys. Rev. E* **99** (1), 012610.

JEFFERY, G. B. 1922 The motion of ellipsoidal particles immersed in a viscous fluid. *Proc. R. Soc. Lond.* **102** (715), 161–179.

JIANG, W. & CHEN, G. 2019a Dispersion of active particles in confined unidirectional flows. *J. Fluid Mech.* **877**, 1–34.

JIANG, W. & CHEN, G. 2019b Solute transport in two-zone packed tube flow: long-time asymptotic expansion. *Phys. Fluids* **31** (4), 043303.

JIANG, W. Q. & CHEN, G. Q. 2018 Solution of Gill's generalized dispersion model: solute transport in Poiseuille flow with wall absorption. *Intl J. Heat Mass Transfer* **127**, 34–43.

KANTSLER, V., DUNKEL, J., POLIN, M. & GOLDSTEIN, R. E. 2013 Ciliary contact interactions dominate surface scattering of swimming eukaryotes. *Proc. Natl Acad. Sci. USA* **110** (4), 1187–1192.

KESSLER, J. O. 1984 Gyrotactic buoyant convection and spontaneous pattern formation in algal cell cultures. In *Nonequilibrium Cooperative Phenomena in Physics and Related Fields* (ed. M. G. Velarde), pp. 241–248. Springer.

KESSLER, J. O. 1985 Hydrodynamic focusing of motile algal cells. *Nature* **313** (5999), 218–220.

KESSLER, J. O. 1986 Individual and collective fluid dynamics of swimming cells. *J. Fluid Mech.* **173**, 191–205.

LEAL, L. G. & HINCH, E. J. 1972 The rheology of a suspension of nearly spherical particles subject to Brownian rotations. *J. Fluid Mech.* **55** (4), 745–765.

LIAO, Q., LI, L., CHEN, R. & ZHU, X. 2014 A novel photobioreactor generating the light/dark cycle to improve microalgae cultivation. *Bioresour. Technol.* **161**, 186–191.

LUSHI, E., KANTSLER, V. & GOLDSTEIN, R. E. 2017 Scattering of biflagellate microswimmers from surfaces. *Phys. Rev. E* **96** (2), 023102.

LUSHI, E., WIOLAND, H. & GOLDSTEIN, R. E. 2014 Fluid flows created by swimming bacteria drive self-organization in confined suspensions. *Proc. Natl Acad. Sci. USA* **111** (27), 9733–9738.

MANELA, A. & FRANKEL, I. 2003 Generalized Taylor dispersion in suspensions of gyrotactic swimming micro-organisms. *J. Fluid Mech.* **490**, 99–127.

MARCHETTI, M. C., JOANNY, J. F., RAMASWAMY, S., LIVERPOOL, T. B., PROST, J., RAO, M. & SIMHA, R. A. 2013 Hydrodynamics of soft active matter. *Rev. Mod. Phys.* **85** (3), 1143–1189.

MARTIN, M., BARZYK, A., BERTIN, E., PEYLA, P. & RAFAI, S. 2016 Photofocusing: light and flow of phototactic microswimmer suspension. *Phys. Rev. E* **93** (5), 051101.

MATA, T. M., MARTINS, A. A. & CAETANO, N. S. 2010 Microalgae for biodiesel production and other applications: a review. *Renew. Sustain. Energy Rev.* **14** (1), 217–232.

MATHIJSSEN, A. J. T. M., SHENDRUK, T. N., YEOMANS, J. M. & DOOSTMOHAMMADI, A. 2016 Upstream swimming in microbiological flows. *Phys. Rev. Lett.* **116** (2), 028104.

MESSIAH, A. 2014 Appendix C. Vector addition coefficients and rotation matrices. In *Quantum Mechanics*, Unabridged reprint edn., pp. 1053–1078. Dover.

MUÑOZ, R. & GUIEYSSE, B. 2006 Algal–bacterial processes for the treatment of hazardous contaminants: a review. *Water Res.* **40** (15), 2799–2815.

NAMBIAR, S., PHANIKANTH, S., NOTT, P. R. & SUBRAMANIAN, G. 2019 Stress relaxation in a dilute bacterial suspension: the active–passive transition. *J. Fluid Mech.* **870**, 1072–1104.

OLVER, F. W. J., LOZIER, D. W., BOISVERT, R. F. & CLARK, C. W. (Eds) 2010 *NIST Handbook of Mathematical Functions*. Cambridge University Press.

PEDLEY, T. J. 2010a Collective behaviour of swimming micro-organisms. *Exp. Mech.* **50** (9), 1293–1301.

PEDLEY, T. J. 2010b Instability of uniform micro-organism suspensions revisited. *J. Fluid Mech.* **647**, 335–359.

PEDLEY, T. J., HILL, N. A. & KESSLER, J. O. 1988 The growth of bioconvection patterns in a uniform suspension of gyrotactic micro-organisms. *J. Fluid Mech.* **195**, 223–237.

PEDLEY, T. J. & KESSLER, J. O. 1990 A new continuum model for suspensions of gyrotactic micro-organisms. *J. Fluid Mech.* **212**, 155–182.

PEDLEY, T. J. & KESSLER, J. O. 1992 Hydrodynamic phenomena in suspensions of swimming microorganisms. *Annu. Rev. Fluid Mech.* **24** (1), 313–358.

POSTEN, C. 2009 Design principles of photo-bioreactors for cultivation of microalgae. *Eng. Life Sci.* **9** (3), 165–177.

RISKEN, H. 1996 Fokker–Planck equation. In *The Fokker–Planck Equation: Methods of Solution and Applications*, 2nd edn. pp. 63–95. Springer.

ROTHSCHILD, N. 1963 Non-random distribution of bull spermatozoa in a drop of sperm suspension. *Nature* **198** (4886), 1221–1222.

RUSCONI, R., GUASTO, J. S. & STOCKER, R. 2014 Bacterial transport suppressed by fluid shear. *Nat. Phys.* **10** (3), 212–217.

RUSCONI, R. & STOCKER, R. 2015 Microbes in flow. *Curr. Opin. Microbiol.* **25**, 1–8.

SAINTILLAN, D. 2018 Rheology of active fluids. *Annu. Rev. Fluid Mech.* **50** (1), 563–592.

SANTAMARIA, F., DE LILLO, F., CENCINI, M. & BOFFETTA, G. 2014 Gyrotactic trapping in laminar and turbulent Kolmogorov flow. *Phys. Fluids* **26** (11), 111901.

STEPHENSON, A. L., KAZAMIA, E., DENNIS, J. S., HOWE, C. J., SCOTT, S. A. & SMITH, A. G. 2010 Life-cycle assessment of potential algal biodiesel production in the United Kingdom: a comparison of raceways and air-lift tubular bioreactors. *Energy Fuels* **24** (7), 4062–4077.

STRAND, S. R. & KIM, S. 1992 Dynamics and rheology of a dilute suspension of dipolar nonspherical particles in an external field. Part 1. Steady shear flows. *Rheol. Acta* **31** (1), 94–117.

SURESH KUMAR, K., DAHMS, H.-U., WON, E.-J., LEE, J.-S. & SHIN, K.-H. 2015 Microalgae – a promising tool for heavy metal remediation. *Ecotoxicol. Environ. Saf.* **113**, 329–352.

TAYLOR, G. 1953 Dispersion of soluble matter in solvent flowing slowly through a tube. *Proc. R. Soc. Lond.* **219** (1137), 186–203.

TAYLOR, G. 1954 The dispersion of matter in turbulent flow through a pipe. *Proc. R. Soc. Lond.* **223** (1155), 446–468.

VOLPE, G., GIGAN, S. & VOLPE, G. 2014 Simulation of the active Brownian motion of a microswimmer. *Am. J. Phys.* **82** (7), 659–664.

WANG, P. & CHEN, G. Q. 2017 Basic characteristics of Taylor dispersion in a laminar tube flow with wall absorption: exchange rate, advection velocity, dispersivity, skewness and kurtosis in their full time dependance. *Intl J. Heat Mass Transfer* **109**, 844–852.

WU, Z. & CHEN, G. Q. 2014 Approach to transverse uniformity of concentration distribution of a solute in a solvent flowing along a straight pipe. *J. Fluid Mech.* **740**, 196–213.

YANG, Y., TAN, S. W., ZENG, L., WU, Y. H., WANG, P. & JIANG, W. Q. 2020 Migration of active particles in a surface flow constructed wetland. *J. Hydrol.* **582**, 124523.

ZENG, L. & PEDLEY, T. J. 2018 Distribution of gyrotactic micro-organisms in complex three-dimensional flows. Part 1. Horizontal shear flow past a vertical circular cylinder. *J. Fluid Mech.* **852**, 358–397.

ZENG, L., ZHANG, H. W., WU, Y. H., LI, C. F. & WANG, P. 2019 Theoretical and numerical analysis of vertical distribution of active particles in a free-surface wetland flow. *J. Hydrol.* **573**, 449–455.

ZÖTTL, A. & STARK, H. 2012 Nonlinear dynamics of a microswimmer in Poiseuille flow. *Phys. Rev. Lett.* **108** (21), 218104.

ZÖTTL, A. & STARK, H. 2013 Periodic and quasiperiodic motion of an elongated microswimmer in Poiseuille flow. *Eur. Phys. J.* E **36** (1), 4.